NASA CR 114,731

INVESTIGATION OF ARTERIAL GAS OCCLUSIONS

by E. W. Saaski

March 1974

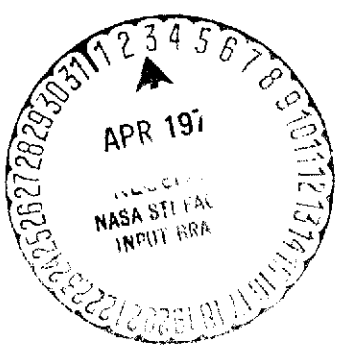

Prepared under Contract No. NAS2-7596 by
Donald W. Douglas Laboratories
McDonnell Douglas Astronautics Company
Richland, Washington
for
AMES RESEARCH CENTER
NATIONAL AERONAUTICS AND SPACE ADMINISTRATION

NASA CR 114,731

INVESTIGATION OF ARTERIAL GAS OCCLUSIONS

by E. W. Saaski
March 1974

Prepared under Contract No. NAS2-7596 by
Donald W. Douglas Laboratories
McDonnell Douglas Astronautics Company
Richland, Washington
for
AMES RESEARCH CENTER
NATIONAL AERONAUTICS AND SPACE ADMINISTRATION

PREFACE

This document is the final report submitted by the Donald W. Douglas Laboratories, a Subdivision of the McDonnell Douglas Astronautics Company, Richland, Washington, under Contract No. NAS2-7596. J. Kirkpatrick was the NASA Technical Manager.

This report covers the period 22 May 1973 through 22 January 1974 and is cataloged as McDonnell Douglas Report MDC G4437.

PRECEDING PAGE BLANK NOT FILMED

CONTENTS

PRECEDING PAGE BLANK NOT FILMED

FIGURES

TABLES

SUMMARY

The effect of noncondensable gases on high-performance arterial heat pipes has been investigated both analytically and experimentally. Models have been generated which characterize the dissolution of gases in condensate, and the diffusional loss of dissolved gases from condensate in arterial flow. These processes, and others, have been used to postulate stability criteria for arterial heat pipes under isothermal and non-isothermal condensate flow conditions.

A rigorous second-order gas-loaded heat pipe model, incorporating axial conduction and one-dimensional vapor transport, has been produced and used for thermal and gas studies. A Freon-22 ($CHClF_2$) heat pipe was used with helium and xenon to validate modeling. With helium, experimental data compared well with theory. Unusual gas-control effects with xenon were attributed to high solubility.

Experimental observations of gas occlusions in heat pipe arteries were made using a stainless-steel heat pipe equipped with viewing ports, and the working fluids methanol and ammonia at two temperatures, with gas additives of helium, argon, and xenon. Observations were related to gas transport models.

Section 1
INTRODUCTION

Within the operating range of high-performance heat pipes, the arterial heat pipe is a potentially superior device in terms of heat transfer capability and ease of construction. Unfortunately, the open cross-section of the arterial channel, which provides a high-conductance fluid path, is also highly susceptible to blockage by noncondensable gases which have been intentionally or unintentionally introduced into the heat pipe. Calculations indicate gas levels in the 10 to 100 parts per million range are sufficient to cause heat pipe failure by initiating arterial depriming.

Up to this time, there was no quantitative model describing the behavior of arterial occlusions under the diverse, non-isothermal conditions within a heat pipe. The objective of this program was to generate valid models describing the response of arterial occlusions to typical heat pipe dynamic transients and steady-state operating conditions.

Analytical modeling has led to expressions describing occlusion movement in response to fluid flow, and the growth of occlusions in response to static and hydrodynamic pressure constraints. Expressions have been derived to estimate gas dissolution in condensate for condensate subcooling and for interaction of these two mechanisms in defining long-term arterial stability.

To verify modeling and experimentally define the dynamic response of an occlusion to flow conditions within a heat pipe, a 90-cm long, 1.27-cm inside diameter, stainless-steel, arterial heat pipe was designed and constructed. The heat pipe incorporated viewing ports in the evaporator and adiabatic transport sections to permit visual observation of occlusion dynamics with a minimum disruption of heat pipe function. In addition to ported pipe experiments, a gas-loaded R-22 ($CHClF_2$) heat pipe was used to experimentally verify a new one-dimensional model describing the stagnant condenser zone in gas-controlled heat pipes. This modeling was essential to estimate gas saturation levels in return condensate. Modeling was in good agreement with experimental thermal profile.

Experimental observations are also presented of occlusion static and dynamic behavior in a heat pipe artery for helium and argon in the methanol working fluid and for helium, argon, and xenon in the ammonia working fluid.

The sections which follow present an analytical summary of the work, description of experimental techniques, and results obtained. Symbols in this report are defined in Section 5.

Section 2
ANALYSIS

Various simultaneous dynamic processes occurring in an operationg heat pipe have been analyzed in terms of component and integral affects on the stability of occlusions in arterial heat pipes. The movement of occlusions at start-up resulting from fluid flow has been expressed in terms of pressure drops around the occlusion and a retarding force attributable to non-equal advancing and receding contact angles. For simplistic screened heat pipes, the secondary wicking permeability is generally low, and only a few watts are necessary to initiate movement. For pressure-primed heat pipes, the secondary wicking is of higher permeability and occlusions may not move as readily. In both instances, as the occlusion is swept towards the evaporator, an elongation may occur as the occlusion moves into fluid regions of lower absolute pressure.

Occlusion movement is discussed in Section 2.1. Interaction of the occlusion with heat pipe pressure fields is discussed in Section 2.2. Once an occlusion is sited within the evaporator, the occlusion elongates and further deprimes the arterial cross-section. Elongation behavior is characterized under differing boundary conditions of gas content and elongation rate.

Section 2.3 and 2.4 analyze the complex interaction of gas dissolution and gas profiles in the condenser with fluid sub-cooling, based on condenser gas zone modeling developed in Appendix A to obtain quantitative values for these processes. That is, condensate returning to the evaporator is laden with dissolved gases picked up in the condensation process, and is also sub-cooled because it has resided for some time in contact with a cold condenser wall. The subcooling concentrates noncondensable gases in the occlusion end cap nearest the condenser. This concentration effect enhances diffusive loss of gas into the condensate. The utility of this process is qualified by the dissolved gases already in the liquid, and an instability factor g^* is derived which quantitatively predicts whether the heat pipe is in a stable mode of operation with a sub-cooled occlusion. Experiments indicate that heat pipes must be operated at very high power levels (without significant assistance of

the artery for fluid pumping) to ensure diffusive collapse. At present, sub-cooling is not practical in pressure-primed heat pipes, unless augmented cooling is used as described by Kosson, et al (Reference 1).

At low power levels, sub-cooling has no beneficial effect, and occlusion size is primarily dominated by pressure drops, gas uptake from returning condensate, and diffusive loss through surrounding fluid films. As discussed in Reference 2, loss processes dominated by fluid diffusion require relatively long times to reach completion.

In the analytical discussions which follow, the term "secondary wicking" is used. This is defined as all axial flow paths, other than the artery, which pump fluid to the evaporator, including wall wicking, stem wicking, and fillets.

2.1 OCCLUSION MOVEMENT

When heat is applied to an initially stagnant heat pipe with an arterial occlusion, fluid flow around the bubble in the arterial wicking produces a pressure drop. For example, if the bubble is initially in the adiabatic section, this pressure drop is given as

$$\Delta P = \frac{M}{K_{ps} A_s} \frac{\mu Q}{h_{fg}} \cdot \ell_b \qquad (1)$$

The effect of this pressure differential is to move the bubble toward the evaporator. As discussed by Schwartz, et.al. (Reference 2), a specific minimum force is necessary to move a gas/liquid/solid interface with a given contact angle and fluid surface tension. This is expressed in the form of a critical force per unit length of contact as $CLF = \gamma/2 (\cos \theta_r - \cos \theta_a)$ where CLF is the critical line force for movement, γ is fluid surface tension, and θ_a and θ_r are the advancing and receding dynamic contact angles, respectively.

For a general gas/liquid/solid triad, an elongated bubble is position stable if the heat transported is less than a factor given as

$$Q_{crit} \leq \frac{A_s \rho K_{ps} h_{fg} \gamma (\cos \theta_r - \cos \theta_a)}{M \mu \ell_b r_a} \qquad (2)$$

A sample calculation was done for ammonia at 20°C. Artery radius was 0.0794 cm, the secondary wicking was assumed to be 2 layers of 200-mesh square-weave stainless-steel screen, with the total cross-section equal to 0.10 cm^2, and K_{ps} equal to 6.2 (10^{-7}) cm^2. Assuming a worst-case contact angle factor of 1.0, the critical heat transfer rate was 5.6 w for a 1.0-cm elongated bubble. This is a low power level. Although the values used to establish CLF are somewhat arbitrary, the general conclusion is that occlusion movement is possible at relatively low power levels.

While possible, movement may not occur if the occlusion elongates in response to other system pressure constraints, or the secondary wicking has a high $K_{ps} A_s$. General pressure constraints are discussed in the following section, the effects of nonisothermality in Section 2.4, and experimental observations in Section 3.

2.2 OCCLUSION BEHAVIOR IN ISOTHERMAL FLOW

In many heat pipes operated at low condensate flow and/or with small cross-section arterial structures, return flow can be assumed in thermal equilibrium with countercurrent vapor flow, and the dynamics assumed to be based on an isothermal system. In this section, the response of an occlusion to flow in an isothermal environment is discussed in terms of occlusion size change with variation in flow or heat transport.

For purposes of discussion, consider an occlusion lodged in the evaporator end of a simple artery as in Figure 2-1, with the heat pipe stagnant. As heat is applied, the occlusion lengthens within the physical constraints of species conservation and hydrodynamic pressure drops. This section describes this interaction for gas/liquid systems which are sparingly soluble.

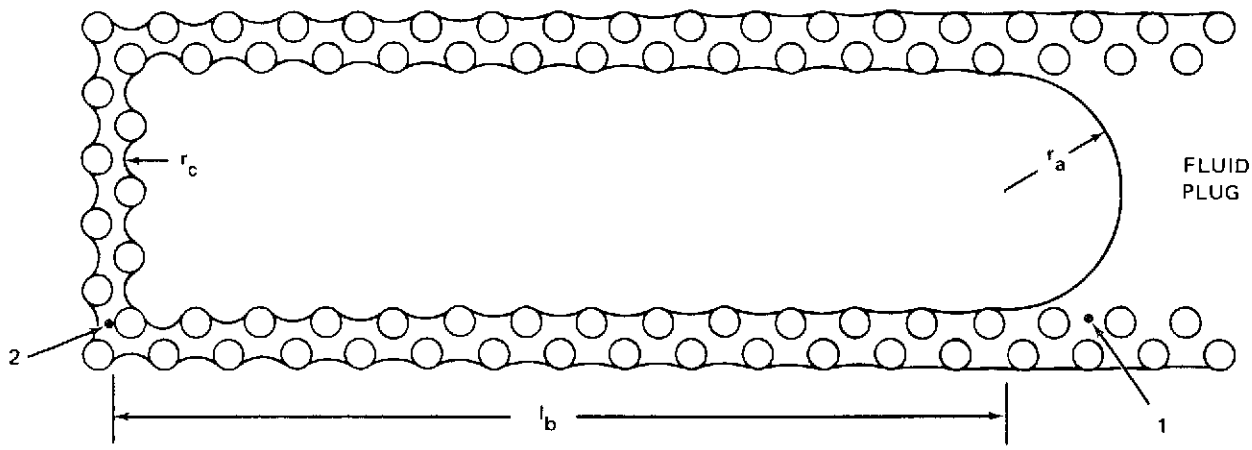

Figure 2-1. Film Recession Around an Arterial Occlusion

2.2.1 Vapor Phase Pressure Constraints

Once the heat pipe is transferring some minimum amount of heat, the initially dispersed gas phase is concentrated into the condenser region and the remainder of the pipe vapor core has a considerably lower mole fraction of gas, assuming no axial pressure variations in the vapor phase. Condensate returning to the evaporator carries with it dissolved gas at the mole fraction $\eta X_{g\ell}$, where η is a factor less than 1.0 representing diffusive loss enroute to the evaporator and $X_{g\ell}$ is the initial mole fraction at the condenser. A simple gas species balance at the evaporator fluid/vapor interface shows that, for uniform vapor composition, the mole fraction of gas in the vapor phase approximately equals the mole fraction in the liquid phase. If gas law deviations are small, so that vapor pressure may be substituted for fugacity, (Reference 4), and mass flux rates are relatively low, then the total pressure in the general vapor phase is given by Raoult's Law as

$$P_a \cong P_{vs}(1 - X'_{g\ell})/(1 - X'_{g\ell}) = P_{vs} \qquad (3)$$

where $X'_{g\ell} = \eta X_{g\ell}$. Within the arterial occlusion, under isothermal conditions, mass transfer is slow enough that equilibrium conditions can be assumed, and the stipulation of equal mole fraction of gas in each phase is not necessary. Therefore,

$$P_b \cong P_{vs} + (K_h - P_{vs}) X_{g\ell} \tag{4}$$

If the two systems were connected, there would be a small pressure difference

$$P_b - P_a = (K_h - P_{vs}) X'_{g\ell} \tag{5}$$

In general, the Henry's Law constant K_h, is much larger than most usually encountered vapor pressures so that the pressure differential is essentially the partial pressure of noncondensable gas within the occlusion, and

$$P_b - P_a = K_h X_{g\ell} \tag{6}$$

Therefore, if a pore in the arterial wicking were to open, noncondensable gas evolves into the general vapor space.

2.2.2 Hydrodynamic Pressure Constraints

However, the fluid film within the arterial wicking prevents this from occurring under most conditions and also determines dynamic response of the occlusion through hydrodynamic pressure drops created by capillarity. The pressure drop in pumping fluid to point "2" (Figure 2-1) from the condenser is

$$\Delta P_{c2} = \Delta P_{c1} + \Delta P_{12} = \Delta P_{a2} \tag{7}$$

The pressure difference ΔP_{a2} is with respect to the general vapor phase under the assumption of an infinite condenser radius of curvature. If it is assumed the fluid/vapor interface within the artery at point "1" is hemispherical, then the pressure differential between the fluid at point "2" and the occlusion vapor core is

$$P_{b2} = \Delta P_{12} + 2\gamma/r_a \tag{8}$$

2.2.3 Occlusion Growth on Start-up

With the basic relationships given in Sections 2.2.1 and 2.2.2, one additional condition is necessary to complete a model describing occlusion behavior during start-up.

Prior to start-up, assume occlusion introduction into the artery as the result of burn-out, adverse tilt, vibration, etc. The initial concentration of gas within the occlusion can be given as $\zeta P_a + 2\gamma/r_a$, reflecting the noncondensable gas concentration in the vapor and the compression effect of surface tension. If the start-up transient is rapid, the amount of noncondensable gas is maintained constant, and for conservation of species,

$$\ell_o (\zeta P_a + 2\gamma/r_a) = P_{gl}\ell_b \tag{9}$$

Because both hydrodynamic pressure constraints and gas conservation occur simultaneously, combining Equation 9 with Equations 6, 7, and 8, produces

$$\ell_o (\zeta P_a + 2\gamma/r_a) = \ell_b \left(\frac{2\gamma}{r_a} - \Delta P_{cl}\right) \tag{10}$$

This is the basic governing equation describing occlusion growth, when growth occurs over a short period relative to the reestablishment of equilibrium gas concentration.

Where start-up is slow, it is possible for noncondensable gases dissolved in returning condensate to establish an equilibrium concentration of gas in the occlusion. For this condition, the governing equations for occlusion length are given by

$$P_{gl} = \frac{2\gamma}{r_a} - \Delta P_{cl} \tag{11}$$

where P_{gl} now is obtained from expressions derived in Sections 2.3 and 2.4 for gas concentration levels in returning condensate, coupled with the gas species equilibrium equation derived in Appendix B. Therefore

$$\ell_b = \frac{v\delta^2}{2D'} \left(C_r^* - \frac{2}{3}\right) \tag{12}$$

C_r^* is defined in Appendix B, and relates to fluid supersaturation.

The final limiting condition for isothermal growth occurs if the initial pressure of noncondensable gas is very small compared to $2\gamma/r_a$. Occlusion length under these conditions is given by

$$\Delta P_{cl} = 2\gamma/r_a \tag{13}$$

From these equations, the primary effect of noncondensable gas is to increase occlusion length above the minimum given by Equation 13. Using

basic assumptions of uniform condensation and evaporation in the condenser and evaporator, and fully developed laminar tube-flow, the pressure drop ΔP_{cl} from the condenser to the point "l" is given by

$$\Delta P_{cl} = \Delta P_{cm} + \Delta P_{am} + \Delta P_{em}(1 - \psi_e^2) \tag{14}$$

$$\Delta P_{cl} = \Delta P_{cm} + \Delta P_{am}(1 - \psi_a) \tag{15}$$

$$\Delta P_{cl} = \Delta P_{cm}(1 - \psi_c)^2 \tag{16}$$

Equations 14, 15, and 16 apply when the bubble extends into the evaporator, adiabatic, and condenser regions of the heat pipe, respectively; ΔP_{cm}, ΔP_{am}, and ΔP_{em} are the pressure drops in completely liquid-filled sections of the condenser, adiabatic, and evaporator regions; ψ_c, ψ_a, and ψ_e represent the fraction of each section containing the bubble. Equations 14, 15, and 16 have been substituted into Equation 10 resulting in two cubic equations for bubble lengths in the evaporator and condenser sections of the heat pipes as well as a quadratic equation for lengths within the adiabatic region. Because of the physically acceptable solutions to ψ_e, ψ_a, and ψ_c, all lying in the range of zero to one, as well as limitations of the physical model, all equations which determine ψ are solved by minimizing the equations while ranging over the interval zero to one in steps of one hundredths. A logic diagram describing the overall numerical program is given in Figure 2-2.

Along the axial length designated ℓ_b in Figure 2-1, the wicking must carry liquid flow to the evaporator surfaces. The pressure drop ΔP_{12} must then reflect conductance of this secondary flow system. This is accommodated by ascribing to the secondary system a relative conductance Z_i, defined as the ratio of the secondary permeability to the arterial conductance. Z_i is considerably less than 1.0 for most systems, and significant pressure drops arise along ℓ_b. Film rupture occurs in this region if the pressure differential across any vapor/liquid interface exceeds the capillary limit $2\,Y/r_c$.

There are two conditions to be considered when the liquid film around the bubble breaks: (1) the fluid film ruptures from the inside to outside (Equation 8) and (2) the capillary pumping demand first deprimes the external wicking layer (Equation 7). If the pressure drop across that part of the artery filled

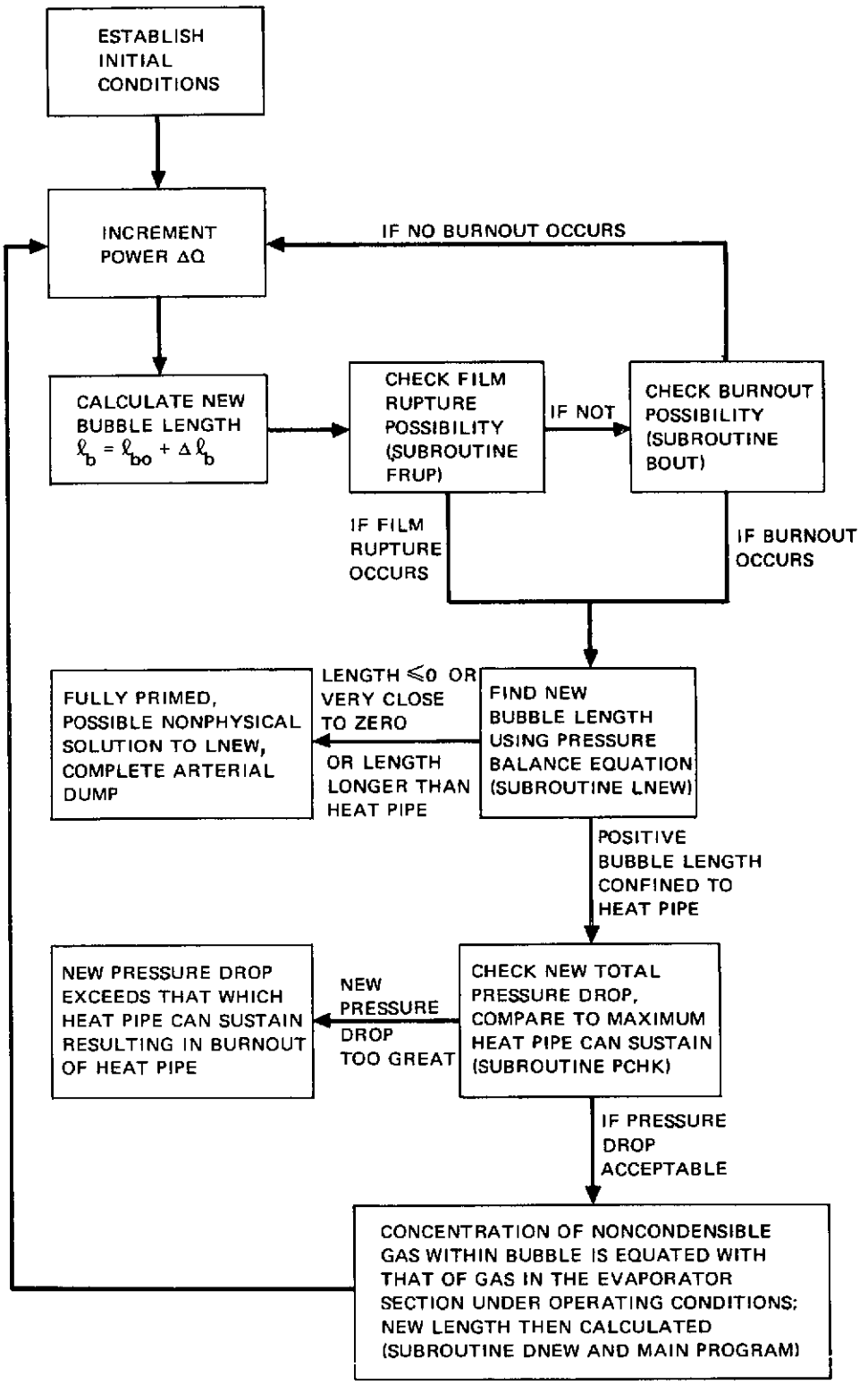

Figure 2-2. Computer Logic Diagram for Occlusion in Isothermal Artery During Startup

with liquid added to the pressure drop across that part of the artery filled with the bubble exceeds $\frac{2\gamma}{r_c}$, then the film around the bubble bursts and heat pipe burnout occurs. Conversely, if the pressure drop across the bubble-filled portion of the artery plus $\frac{2\gamma}{r_a}$ exceeds $\frac{2\gamma}{r_c}$, then the film of liquid again ruptures but gas is forced from the bubble into the vapor space until a pressure balance ensues, and burnout does not necessarily occur. If an artery film ruptures because of Equation 8, a new, shorter-length occlusion results where

$$\Delta P_{c1} = 2\gamma/r_a \tag{17}$$

If the fluid film "heals" and the new pressure drops prove to be compatible with heat pipe pumping capabilities, subsequent lengths of the bubble as a function of power may be calculated using Equation 17. The use of this equation in describing further occlusion length change assumes that all noncondensable gas in excess of the general vapor-phase concentration has been vented, and the action of gas in defining occlusion length is now secondary. This may not be a valid assumption under all conditions, but does define a limit to occlusion behavior.

Using the model based on Equations 10 and 17, Figures 2-3 and 2-4 present calculated occlusion lengths as a function of the fractional fully primed power level for different levels of initial gas content, for two values of secondary wicking relative permeability, and for the parameter $r_c/r_a = 0.10$. In Figure 2-3, the relative permeability of the secondary wicking, Z_i, relative to the artery permeability is 0.67, while in Figure 2-4, the relative permeability is 0.10. In each case, the plots are parameterized in initial reduced noncondensable gas pressure present in the heat pipe prior to start-up, and

$$f = \frac{P_g}{2\gamma/r_a} \tag{18}$$

Initial occlusion length is taken as 0.10 of the evaporator length.

The effect of increased initial gas concentration is to produce rapid depriming by arterial fluid expulsion as gas expands within the artery. If the film rupture phenomena occurs, then the gas content is at least partially expelled; however, the heat pipe ultimately burns out at the same level of relative power independent of initial gas content. The effect of increased secondary wicking permeability

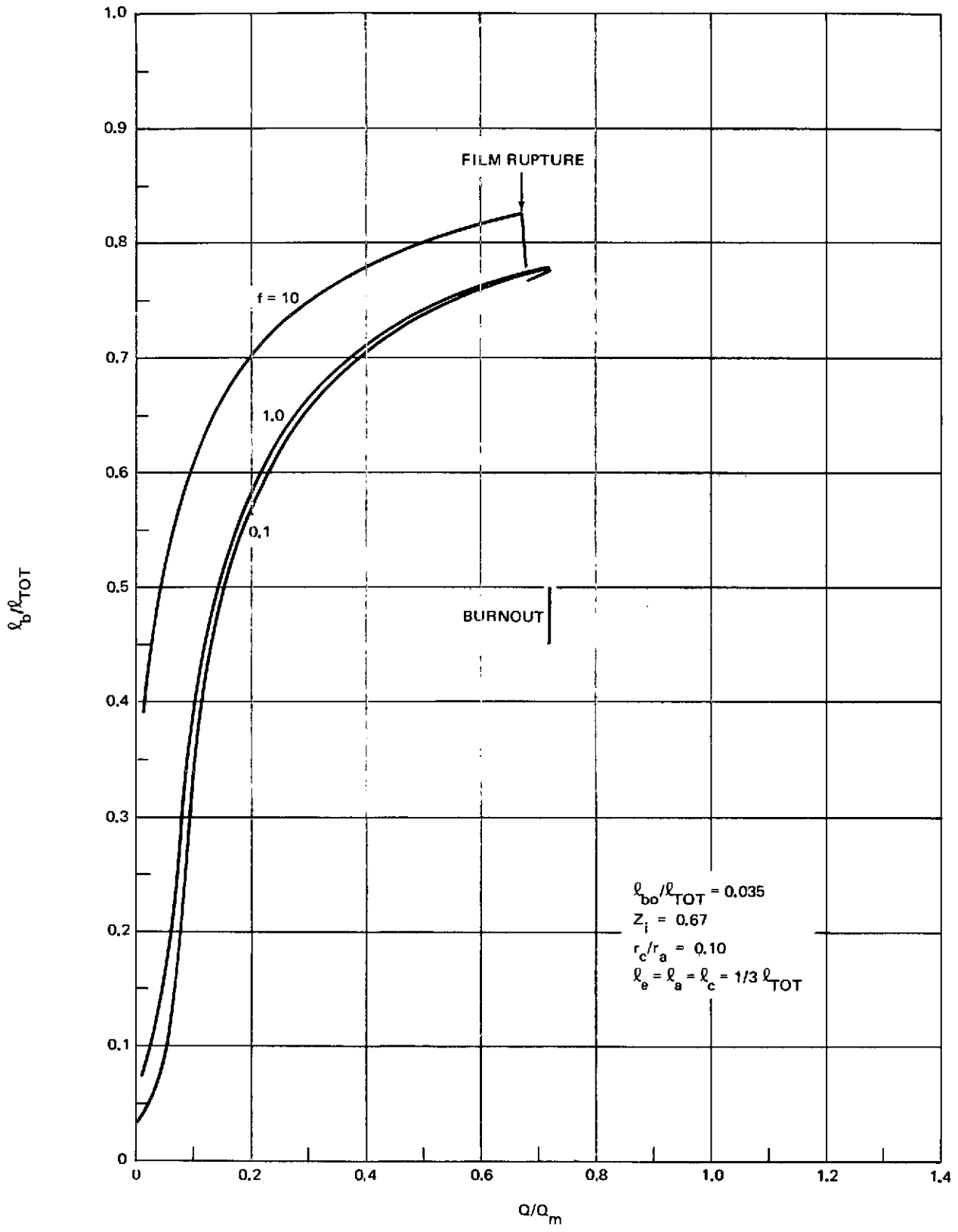

Figure 2-3. Occlusion Elongation as Affected by Gas Pressure Transport Rate, and Secondary Permeability

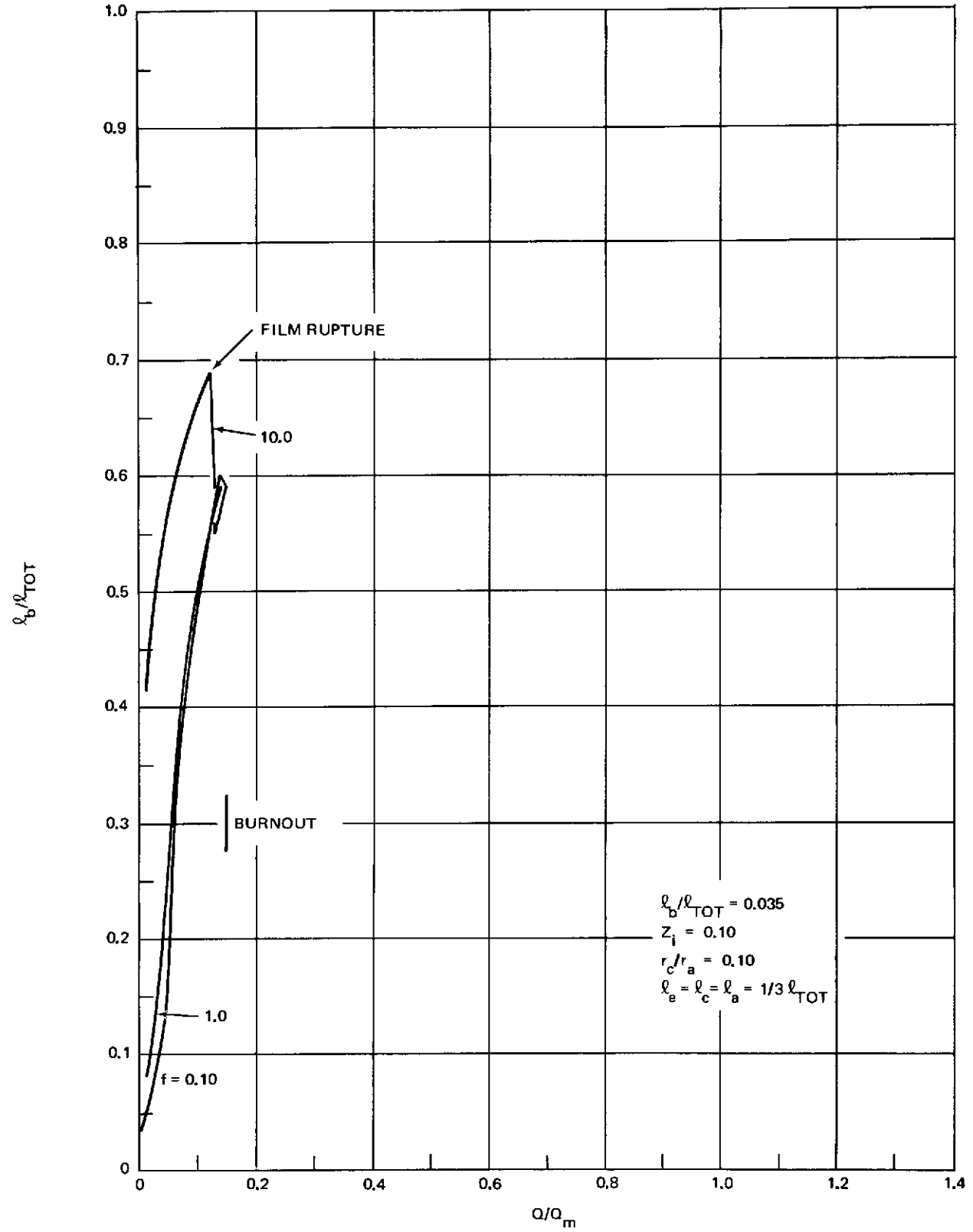

Figure 2-4. Occlusion Elongation as Affected by Gas Pressure, Transport Rate, and Secondary Permeability

is to retard burn-out, but burn-out still appears inevitable as $Q/Q_m \rightarrow 1.0$ for an isothermal system, unless $Z_i \geq 1.0$, at which point, the entire load is sustained by the secondary wicking.

2.2.4 Gravity Effects

In all pressure constraints discussed here, gravity decreases the compressive effect of surface tension as

$$\frac{2\gamma}{r_{eff}} = \frac{2\gamma}{r_a}\left(1 - \frac{\rho g h}{2\gamma/r_a}\right) \tag{19}$$

where h is the height of the uppermost portion of the artery with respect to an infinite fluid pool.

2.3 CONDENSER PHENOMENA

The condenser has influence on the behavior of arterial occlusions. The long-term stability of occlusions is directly dependent on the quantity of noncondensable gas picked up by fluid during condensation, and on the degree of subcooling of the condensate. High levels of gas in return condensate enhance the growth of occlusions by diffusion feeding of gas from liquid to the occlusion vapor phase. Alternatively, condensate subcooling compresses gases within an occlusion so that diffusive loss from the occlusion vapor phase to the flowing condensate is augmented. In this section, models are derived for gas dissolution and condensate subcooling in a gas-loaded heat pipe.

2.3.1 Gas-Zone Modeling

A mathematical model has been derived for the concentration and thermal profiles of a stagnant noncondensable gas zone in a heat pipe (Appendix A includes a detailed discussion of the model). Only axial composition changes are assumed, and solubility of the gas in working fluid is assumed negligible in its effect on mass transfer. The governing differential equations relate conservation of species to axial/radial heat transfer within the heat pipe wall and condensate film and also within any coupled coolant systems.

Because all physical properties change with temperature, the governing second-order non-linear differential equations have been solved by a relaxation technique such that the temperature profiles obtained at each iteration are

used to re-initialize diffusion coefficients, fluid density, and latent heat of vaporization, for example, until a stable set of temperatures and concentrations is obtained.

2.3.2 Gas Dissolution

It has been shown in Appendix A that a condenser gas leg enhances condensation in the diffuse transition zone that separates the primary gas leg from the operating condenser section. Within this zone, condensation is taking place in the presence of noncondensable gas, and it is a reasonable assumption that noncondensable gases which diffuse into the fluid film in this area are eventually carried towards the evaporator. If local equilibrium of gas in the vapor and liquid phases is assumed, then it is possible to estimate the amount of gas transported to the evaporator. In Figure A-9, Curve 3 shows the local gas dissolution rate for the helium/Freon-22 heat pipe; gas dissolution peaks in a relatively narrow range even for the high axial-conductance aluminum-walled heat pipe used in these experiments.

It is a relatively simple matter to numerically integrate rate distribution to obtain the overall dissolution rate if a numerical model is available for the entire condenser system. However, considerable insight can be gained by a simplistic closed-form model for the dissolution process.

In a gas-loaded heat pipe, it has been shown by Marcus (Reference 5) that axial gas leg thermal distributions in many often used gas-fluid systems are dominated by wall conduction into the gas zone. That is, the gas zone acts as a fin connected to the active condenser. The mathematical models describing temperature profiles in a fin closely describe wall profiles in gas-loaded heat pipes. Therefore, it can be expected that fin-type equations describe vapor temperature in the gas zone, and on this basis, a model for dissolution is possible. Figure 2-5 shows typical relations between vapor, wall temperature, and axial position. Temperature distribution along the wall for $z \geq z_o$ can be approximated by the fin equation

$$T_w^* = T_{w1}^* \, \mathrm{EXP}\left(- (z - z_o)/\bar{z} \right) \qquad (20)$$

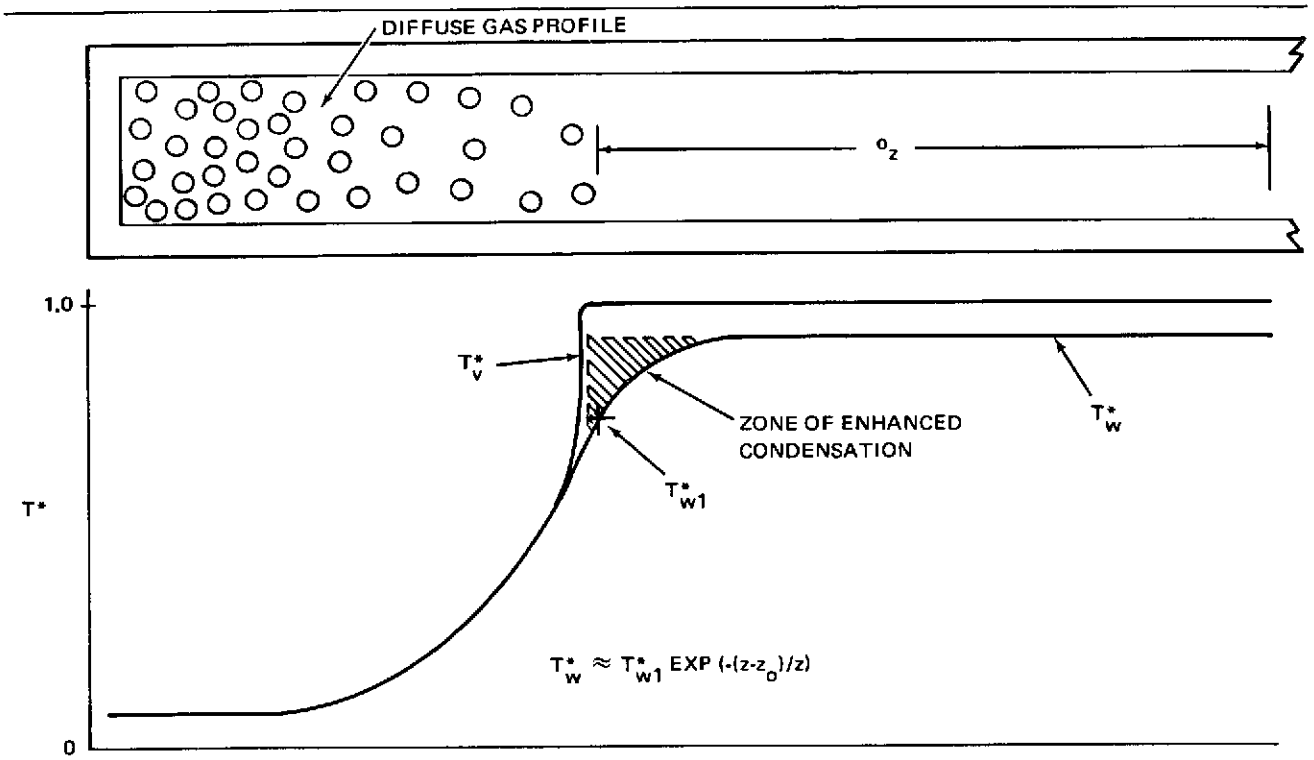

Figure 2-5. Representative Thermal Profiles for a Gas-Loaded Heat Pipe

In the axial zone where most gas is picked up by condensate, the vapor temperature can be expected to roughly follow Equation 20 in functional form, so that

$$T_v^* - T_w^* = \Delta T_{vw}^* \quad \text{EXP} (- (z - z_o)/z') \tag{21}$$

Relating the temperature difference to mass flux by Equation A-1, total mass flow into the gas zone is

$$\dot{n}_v = Q_\ell z'/h_{fg} \tag{22}$$

The Ostwald solubility coefficient is defined as the ratio of mole concentration of gas in the liquid phase to that in the vapor phase. Use of this factor then gives the overall rate of gas dissolution as

$$\dot{n}_g = \frac{\alpha M}{\rho} \quad \frac{C \, \overline{X}_g Q_\ell z'}{h_{fg}} \tag{23}$$

The average mole fraction of noncondensable gas $\overline{X}_g$ can be estimated from system temperature limits, and because z' must be on the order of $\overline{z}$, it will be replaced by $\overline{z}$. Considering the overall condenser system, and assuming uniform condensation, condensate leaving the condenser has a molar concentration of noncondensable gas given by

$$C_{g\ell} \approx \frac{\alpha C \overline{X}_g \overline{z}}{z_o + \overline{z}} \tag{24}$$

2.3.3 Condensate Subcooling

As discussed in Section 2.3.2, gradients within the stagnant zone of a gas-loaded heat pipe can be described approximately by fin equations. Within the gas-free condenser zone, this is also true. Assuming the heat pipe wall is connected to the vapor phase through a fluid film with conductance G_f, and to a constant temperature sink through a conductance G_i, then the temperature distribution along the wall is given by

$$T_w^* = \frac{\beta}{\lambda^2} \left(1 - \frac{\cosh(\lambda z_w^*)}{\cosh(\lambda z_{ow}^*) + \lambda \sinh(\lambda z_{ow}^*)} \right) \tag{25}$$

The Equation A-9 has been solved with a zero-derivative boundary condition at $z = 0$, and with fin-coupling boundary conditions at the gas zone interface $z = z_o$. For the coupled gas-zone fin, Equation 20 was used.

Under steady state conditions, the local condensation rate (Figure 2-5) is proportional to $1 - T_w^*$, and average condensate subcooling to $1/2\ (1 - T_w^*)$. In Equation 25, if the hyperbolic terms are omitted, the remainder reflects the constant gradient present in the absence of end effects. A condensation subcooling enhancement factor can then be defined by

$$f_c = \frac{1/2 \int_o^{z_{ow}^*} (1 - T_w^*)^2 \, dz^*}{1/2\ (\beta/\lambda^2)^2\ z_{ow}^*} \tag{26}$$

The factor f_c in closed form is

$$f_c = 1 + \frac{\beta^2}{I^2} \left[1/2 + \frac{\sinh(2\lambda z_{ow}^*)}{4\lambda z_{ow}^*} + \frac{2I \sinh(\lambda z_{ow}^*)}{\lambda \beta z_{ow}^*} \right] \tag{27}$$

where $I = \cosh(\lambda z^*_{ow}) + \lambda \sinh(\lambda z^*_{ow})$

Figure 2-6 shows constant enhancement-factor profiles as a function of $\beta = G_f/G_i$ and as a function of the axial dimension factor $\sqrt{G_i/A_w K_w}$ for a condenser with length z_o of 15 cm. An increase in the ratio G_f/G_i increases end effects, as does a decrease in the axial factor $\sqrt{G_i/A_w K_w}$. For the Freon-22 heat pipe described in Appendix A, the average condensate subcooling ΔT is 1.8 times higher than expected without the end effect.

2.4 OCCLUSION BEHAVIOR IN NON-ISOTHERMAL FLOW

Bases for estimating gas dissolution in condensate and condensate subcooling have been presented. These initial values for condenser concentration and temperature are used to estimate the actual fluid concentration and temperature levels present at the occlusion, which in general, will not be in the condenser

2.4.1 Thermal and Mass Transfer in Arterial Flow

The gain of heat and loss of mass from a flowing tube of fluid with a permeable outer surface is described by the same differential equation in the limit of a sparingly soluble gas. The general heat and mass transfer model used is shown in Figure 2-7.

As fluid moves down the tubular artery in fully developed laminar flow, initially constant radial temperature and gas concentration profiles change in shape resulting from loss of gas at the free interface and gain of heat by condensation onto the free surface. Assuming no inverse-transpiration effects occur in the vapor phase, then the dominant thermal and mass transfer resistances occur within the flowing tube and the governing differential equations are to a good approximation

$$V_m \left(1 - \left(\frac{r}{r_a}\right)^2\right) \frac{\partial U}{\partial z} = \theta_{h,m} \frac{\partial}{\partial r}\left(r \frac{\partial U}{\partial r}\right) \qquad \text{(adiabatic)} \qquad (28)$$

$$V_m \left(1 - \left(\frac{r}{r_a}\right)^2\right) \left(1 - \frac{z_e}{\ell_e}\right) \frac{\partial U}{\partial z} = \theta_{h,m} \frac{\partial}{\partial r}\left(r \frac{\partial U}{\partial r}\right) \qquad \text{(evaporator)} \qquad (29)$$

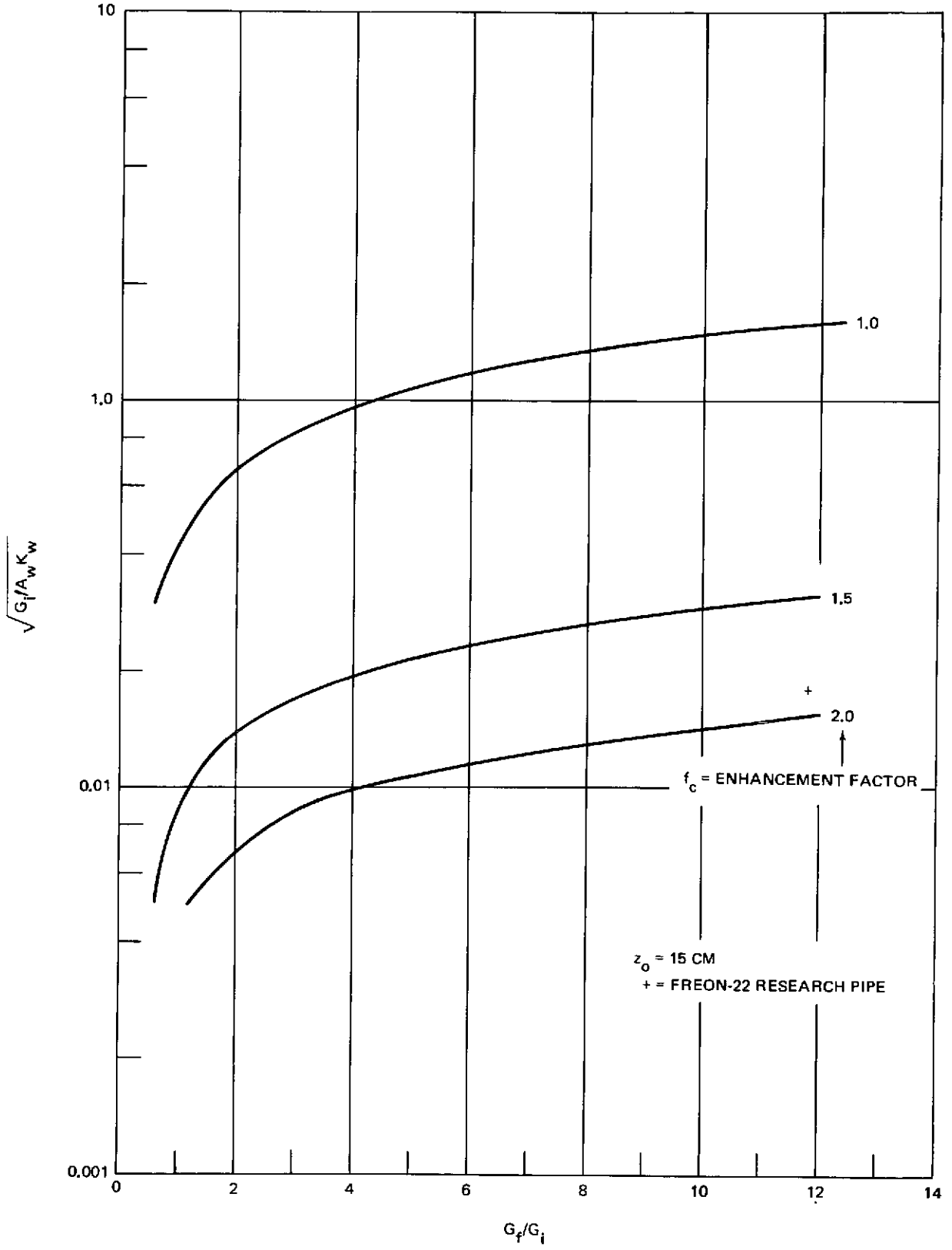

Figure 2-6. Subcooling Enhancement Factor Related to Heat Transfer Properties

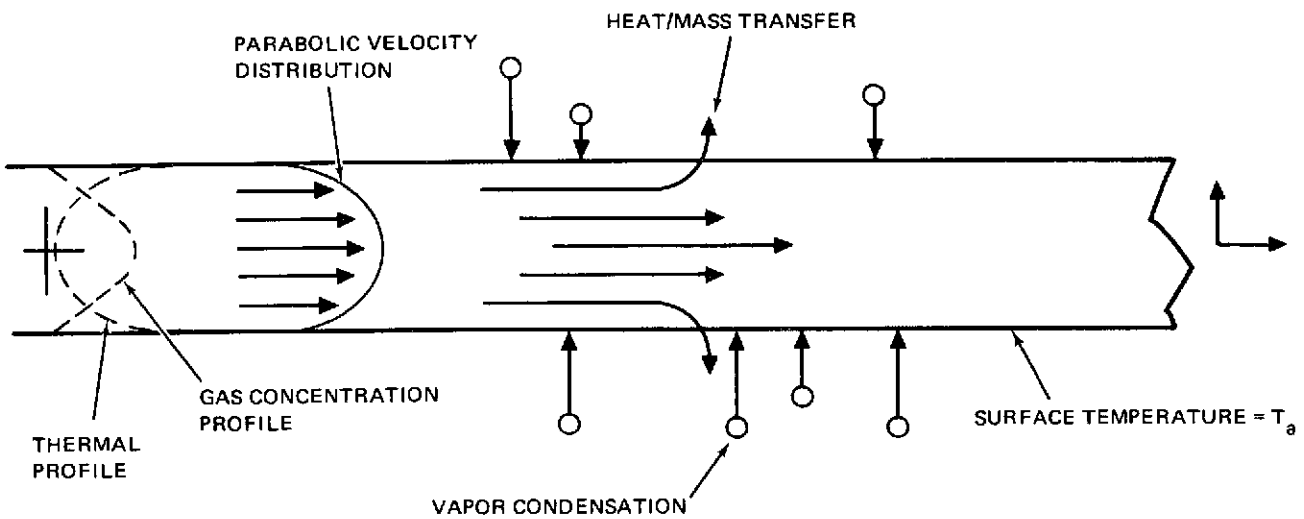

Figure 2-7. General Heat/Mass Transfer Model (Adiabatic Section)

In Equation 29, z_e is measured from the adiabatic/evaporator interface. For heat and mass transfer, the factors θ are

$$\theta_h = K_\ell / \rho C_p ; \qquad \theta_m = D_{g\ell} \tag{30}$$

If the following dimensionless variables are defined, a minimum number of arbitrary constants follow.

$$\psi_e = \frac{z_e}{\ell_e} \qquad U_m = \frac{C_{g\ell} - C_{gv}}{C_{gc} - C_{gv}} \qquad U_h = \frac{T - T_v}{T_c - T_v} \tag{31}$$

$$r^* = \frac{r}{r_a} \qquad \nu = \frac{\theta}{V_m r_a^2} \qquad z^*_{h,m} = \nu z \tag{32}$$

The Equations 28 and 29 are now given as

$$(1-r^{*2}) \frac{\partial U^*}{\partial z^*} = \frac{1}{r^*} \frac{\partial}{\partial r^*} \left(r^* \frac{\partial U^*}{\partial r^*} \right) \tag{33}$$

$$(1-r^*)\ (1-\psi_e) \frac{\partial U^*}{\partial z^*} = \frac{\nu}{r^*} \frac{\partial}{\partial r^*} \left(r^* \frac{U^*}{r^*} \right) \tag{34}$$

Boundary conditions, dropping the asterisk notation, are

$$\frac{\partial U}{\partial r} = 0 \qquad r = 0 \qquad 0 \leq z \tag{35}$$

$$U = 1 \qquad z = 0 \qquad 0 \leq r \leq 1 \tag{36}$$

$$U = 0 \qquad r = 1 \qquad 0 < z \tag{37}$$

Both Equations 33 and 34 have been solved using an implicit numerical technique. However, Equation 34 is difficult to use for general characterization studies because the solution must be parameterized in at least the factor ν. The arbitrary constants are absorbed in Equation 33 into dimensionless factors so that one solution to the differential equation solves all cases. With some reservations, Equation 33 can characterize the entire heat pipe artery if a suitable average flow velocity is used for the condenser and evaporator sections. Alternately, it is difficult to define where $z^* = 0$ actually occurs within the condenser based on the fact that the initial condition $U = 1$ is not strictly accurate because condensate may be uniformly injected into the artery, or there may be a peak in condensation rate as a function of position near the gas zone interface. It is apparent that Equation 33 is most applicable to the total heat pipe when the active condenser length is small in contrast to the total length. The exact solutions to Equation 34 for the evaporator show this approximate method is worst when the occlusion is very short and lodged in the far end of the evaporator. The general effect of using Equation 33 instead of 34 in these cases is to significantly underestimate g^*, a factor defined at later in this section. Therefore, the use of Equation 33 is optimistic in estimation of occlusion stability and collapse.

Figure 2-8 presents the solution to Equation 33 in terms of $\overline{U}$ and $z^*_{h,\,m}$. The dependent variable $\overline{U}$ is the mass-flux weighted dimensionless temperature or gas concentration. This variable was selected for presentation because fluid mixing is likely to occur at the occlusion head as fluid diverts from the cylindrical artery to secondary wicking. The average fluid temperature and gas composition are the important factors in relating non-isothermal flow behavior to occlusion stability. The numerical solution was derived using

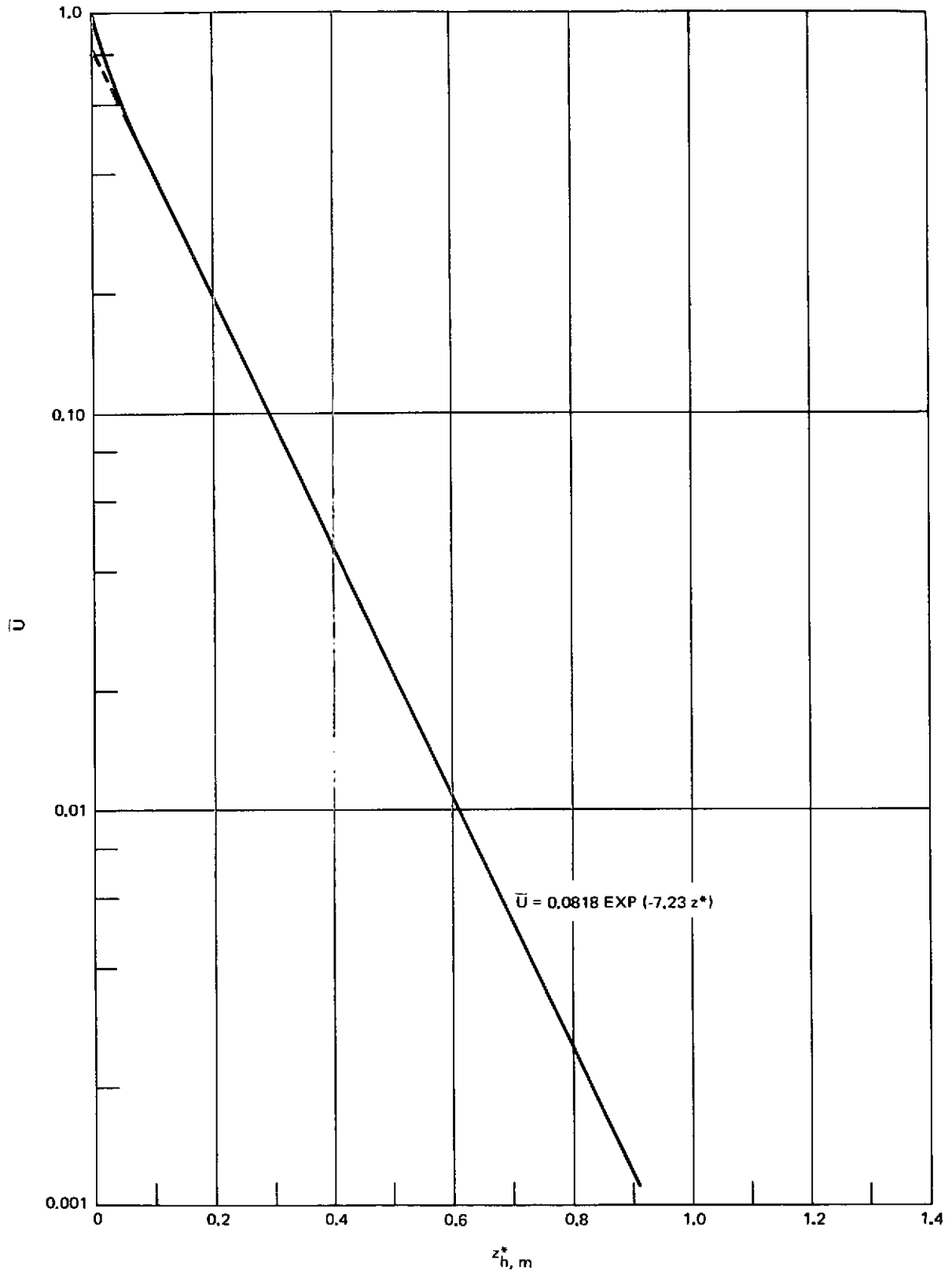

Figure 2-8. Flow-Weighted Average Concentration or Temperature for Tube Flow with a Permeable Surface

0.001 step-size in z^*, and the radial distance was divided into 100 equal parts. The numerical solution very closely fits the empirical expression

$$\bar{U} = 0.818 \text{ EXP } (-7.23 z^*) \qquad z^* > 0.025 \qquad (38)$$

2.4.2 Non-Isothermal Stability

As condensate impinges on the occlusion end cap, the slightly cool condensate creates an accumulation of noncondensable gas at point "1" in Figure 2-1, in analogy with the macroscopic phenomenon in a heat pipe. At the same time, dissolved gas is being transported from the condenser. The compressive effect of temperature enhances gas removal from the occlusion by increasing internal gas concentration which accelerates diffusive loss. In addition, if the occlusion is elongated, diffusive loss may be occurring at an appreciable rate through the fluid-filled arterial wall (Reference 2). Long-term operational stability requires the diffusion and thermal mechanisms to dominate over gas injection from return condensate.

The hydrodynamic pressure constraints given in Section 2.2.2 are not altered by nonisothermal conditions. The pumping capability of the artery with an occlusion is still solely determined by r_c and r_a. However, partial pressure of noncondensable gas is altered.

Vapor pressure depression at the occlusion end-cap is given by the derivative of vapor pressure with temperature multiplied by the difference between coolant and vapor core temperature. Denoting the derivative as P', the total gas pressure at the end cap "1" is

$$P_{g1} = \frac{2\gamma}{r_a} - \Delta P_{c1} + P'\Delta T_1 \qquad (39)$$

For a given amount of noncondensable gas, the temperature effect then serves to compress the occlusion length. In many cases, the first two terms are close to being equal, so that diffusion gradients are primarily determined by $P' \Delta T$. The induced equilibrium gas concentration within the liquid at end cap "1" is

$$C_{g1} = \frac{\alpha P' \Delta T_c \eta(z_h^*)}{RT} \qquad (40)$$

The factor ΔT_c accounts for the initial subcooling derived in Section 2.3.3, while $\eta(z_h^*)$ accounts for condensate thermalization as derived in Section 2.4.1.

The gas condentration attributable to dissolved material from the condenser is

$$C_{g2} = \frac{\alpha P_a \bar{X}_g z \eta(z_m^*)}{(z_o + \bar{z}) RT} \tag{41}$$

As a relative guarantee of stability, Equation 41 must be smaller than Equation 40 to allow diffusive collapse. If the ratio is defined as g^*, manipulation gives

$$g^* = \frac{C_{g2}}{C_{g1}} = \frac{2 G_f \bar{X}_g P_a \eta(z_m^*)}{P' f_c Q \eta(z_h^*)} \sqrt{\frac{K_w A_w}{G_i}} \tag{42}$$

Stability criteria are, therefore, dependent on many of the interacting phenomena. However, the solubility does not appear explicitly. This is related to the fact that there are two gas/liquid interfaces considered, and the dependence cancels out when a ratio is taken.

2.5 NON-ISOTHERMAL STABILITY CALCULATIONS

An expression g^* has been derived which predicts occlusion stability under quite general non-isothermal conditions in a gas-loaded heat pipe (Equation 42). If g^* is less than 1.0, diffusive collapse occurs, while for $g^* > 1$, elongation may occur depending on the absolute level of gas in the supersaturated condensate. Calculations of the factor g^* are given here for the fluids ammonia, Freon-21, and methanol.

For numerical calculations, g^* can be modified into a more tractable form by using the Miller correlation given in Appendix A to express the ratio P'/P_a, with P_a assumed equal to P_{vs}. In addition, the closed-form expression (Equation 38) for η_m and η_h can be substituted into Equation 41 to give the closed-form expressions.

$$g^* = \frac{1.64 G_f \bar{X}_g}{f_c} \sqrt{\frac{K_w A_w}{G_i}} g_f \tag{43}$$

$$g_f = \frac{T_c}{\varepsilon Q} \text{EXP} \left[\frac{-11.35 h_{fg} (\rho D_{g\ell} - K/C_p) z}{MQ} \right] \tag{44}$$

The component expression g_f has been called the fluid instability factor, because remaining terms in Equation 43 are related to specific system design. The expression g^* is actually independent of arterial diameter, so that g_f is appropriate for all simple tubular arteries, within the limits defined in Section 2.4. In addition, the sign of the exponential factor is dependent on the difference between mass and thermal diffusivities.

Using experimental diffusivity data in Reference 2 as a basis, Figures 2-9 and 2-10 show the dependence of g_f on temperature, gas composition, power level, and working fluid for a mean distance z = 100 cm separating the condenser from the occlusion cap. If adequate subcooling is available to maintain arterial priming, then Figures 2-9 and 2-10 show that increasing power level tends to improve the mass transfer balance. The product of factors other than g_f in g* are on the order of 1.0. Therefore, g_f must also be on the order of 1.0, or less, to ensure stability or collapse. However, in the best case, a minimum power level of 590 watts is required for $g_f = 1.0$.

The fluid instability factor decreases with increasing temperature, and is smaller for Freon-21 than for methanol or ammonia. The change with temperature is attributable to increasing diffusion coefficients, and decreasing thermal conductivity, while the principal variation with fluid is created by differences in h_{fg}/M, $D_{g\ell}$, and K/C_p.

In general, however, the predominant mechanism by which g_f decreases is by a power increase. In a standard screened artery, use of this characteristic is impractical because a power increase causes the occlusion to elongate in response to dynamic pressure changes, as shown in Section 2.2. However, when the secondary wicking has a very high permeability and surrounds the central artery, as in a pressure-primed heat pipe, then the subcooling effect may extend the entire length of the occlusion and may be sufficient to arrest occlusion growth.

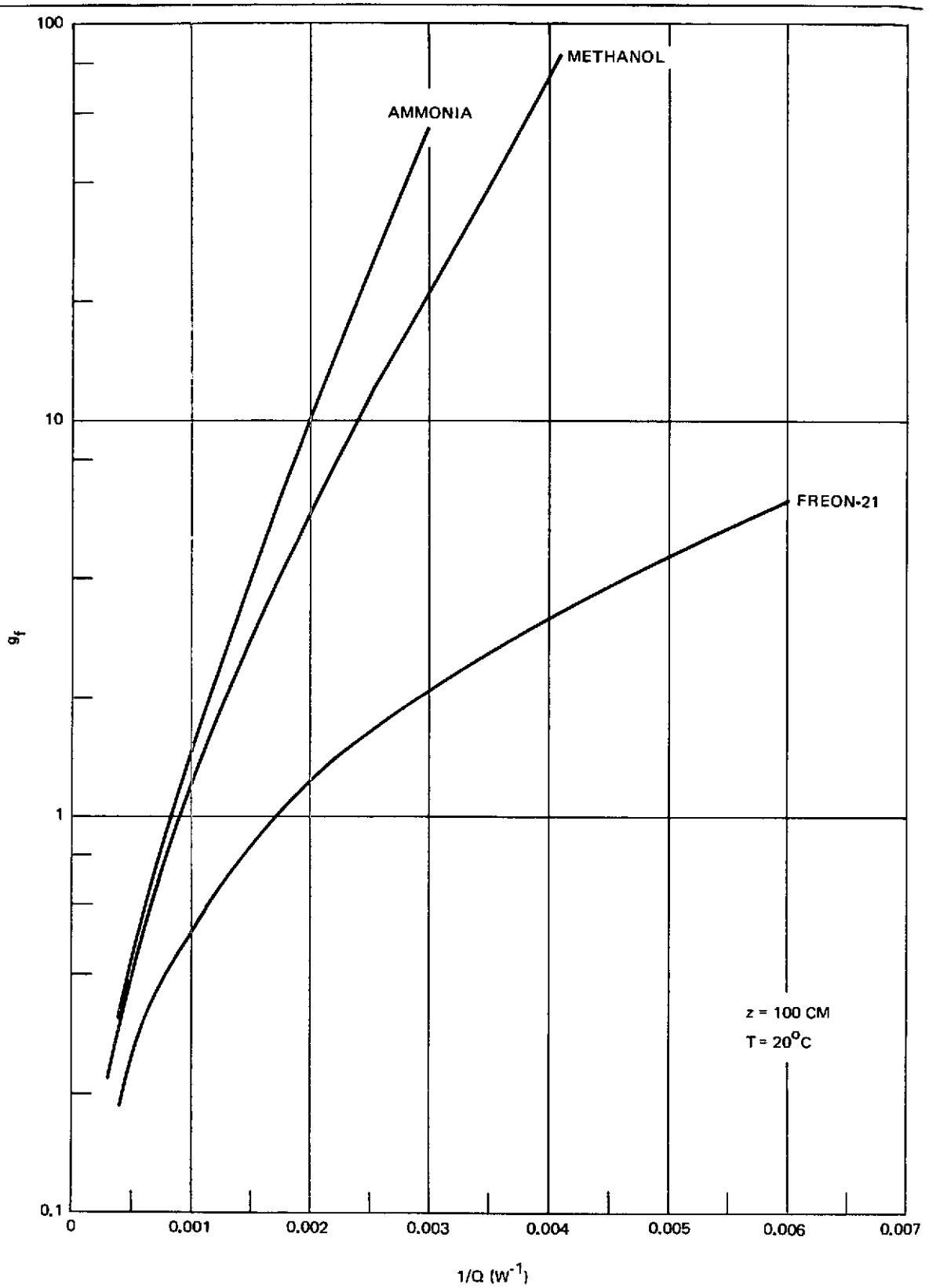

Figure 2-9. Fluid Instability Factor for Three Fluids with Helium Noncondensable Gas

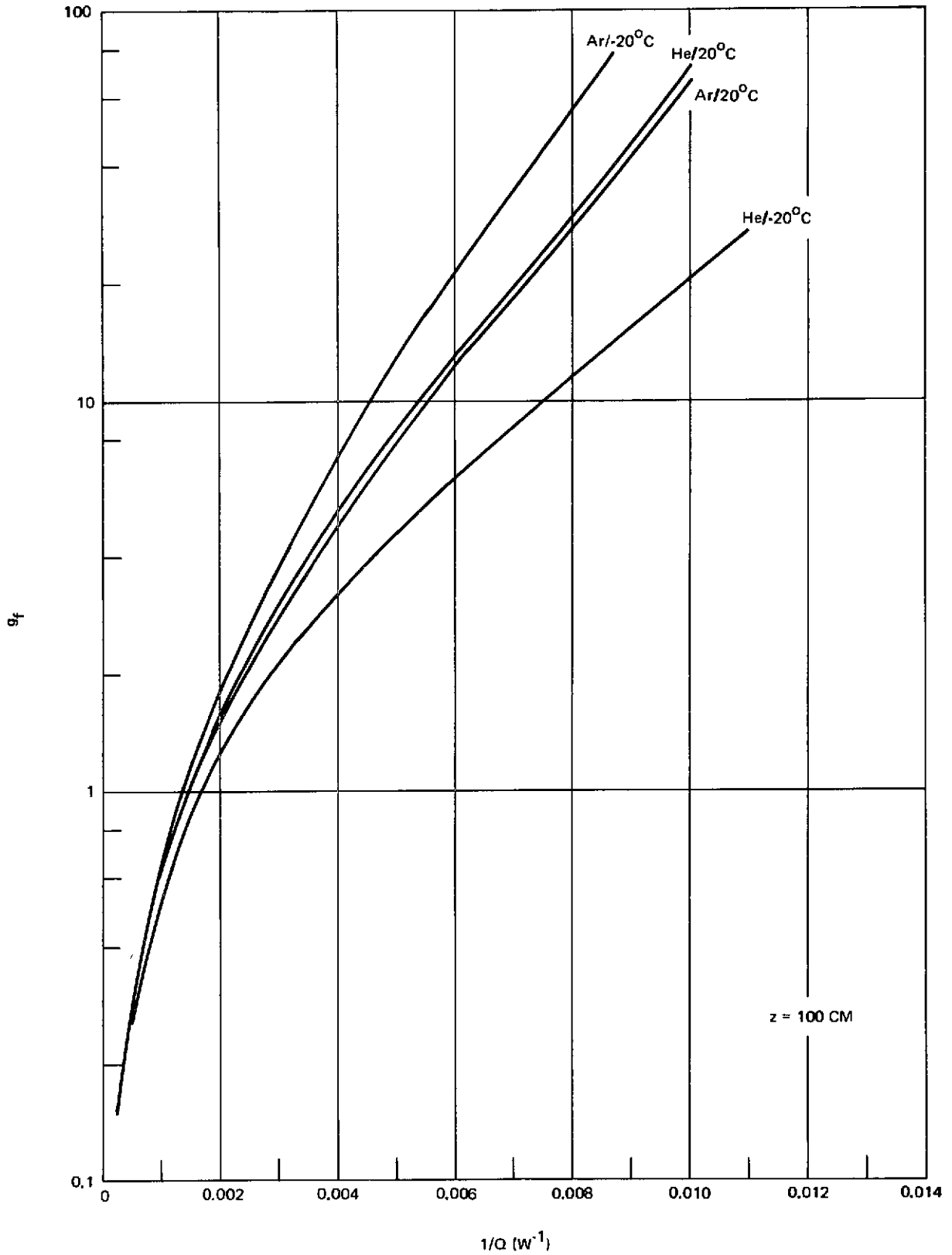

Figure 2-10. Fluid Instability Factor for Freon-21 with Helium and Argon

Section 3
EXPERIMENTAL INVESTIGATION

3.1 EXPERIMENTAL APPARATUS

To study the stability of arterial occlusions in an operating heat pipe, a stainless-steel heat pipe was constructed (Table 3.1, Figure 3.1). The heat pipe was 91.7 cm long, and had a 1.27 cm inside diameter. The heat pipe was designed with three approximately equal lengths for the evaporator, adiabatic section, and condenser. The evaporator and adiabatic sections contained 22 equally spaced viewing slots 2.54 cm long and 0.246 cm wide which were sealed with Buna-N O-rings in compression against optical glass window ports. Slots permitted direct observation of arterial function with minimum disruption to heat pipe operation. In a previous program (Reference 2), observations of arterial behavior in all-glass systems were extremely difficult because of thermal gradients and absorption of radiant energy by the artery structure, both of which affected bubble dissolution rates on a first-order level.

The evaporator end cap also mounts with an O-ring so that instrumentation may be changed at the evaporator end. Both ends are of open cross-section so that diverse wicks and arterial designs may be inserted.

The artery consisted of a screened 0.159-cm inside diameter tube on the heat pipe axis. The tube and a vertical web connecting the artery top and bottom to the walls were constructed of two layers and four layers of 200-mesh stainless-steel screen, respectively. Wicking on the wall consisted of a single layer of the same 200-mesh screen. The pipe was heated by identical resistance heaters on the top and bottom evaporator faces. In the condenser, cooling was accomplished with two identical copper plates bolted to the side faces.

The heat pipe was designed for an operating pressure of 200 psig, so that priming characteristics of high-pressure fluids such as ammonia can be investigated. For tests conducted in this program, ammonia and methanol working fluids were used.

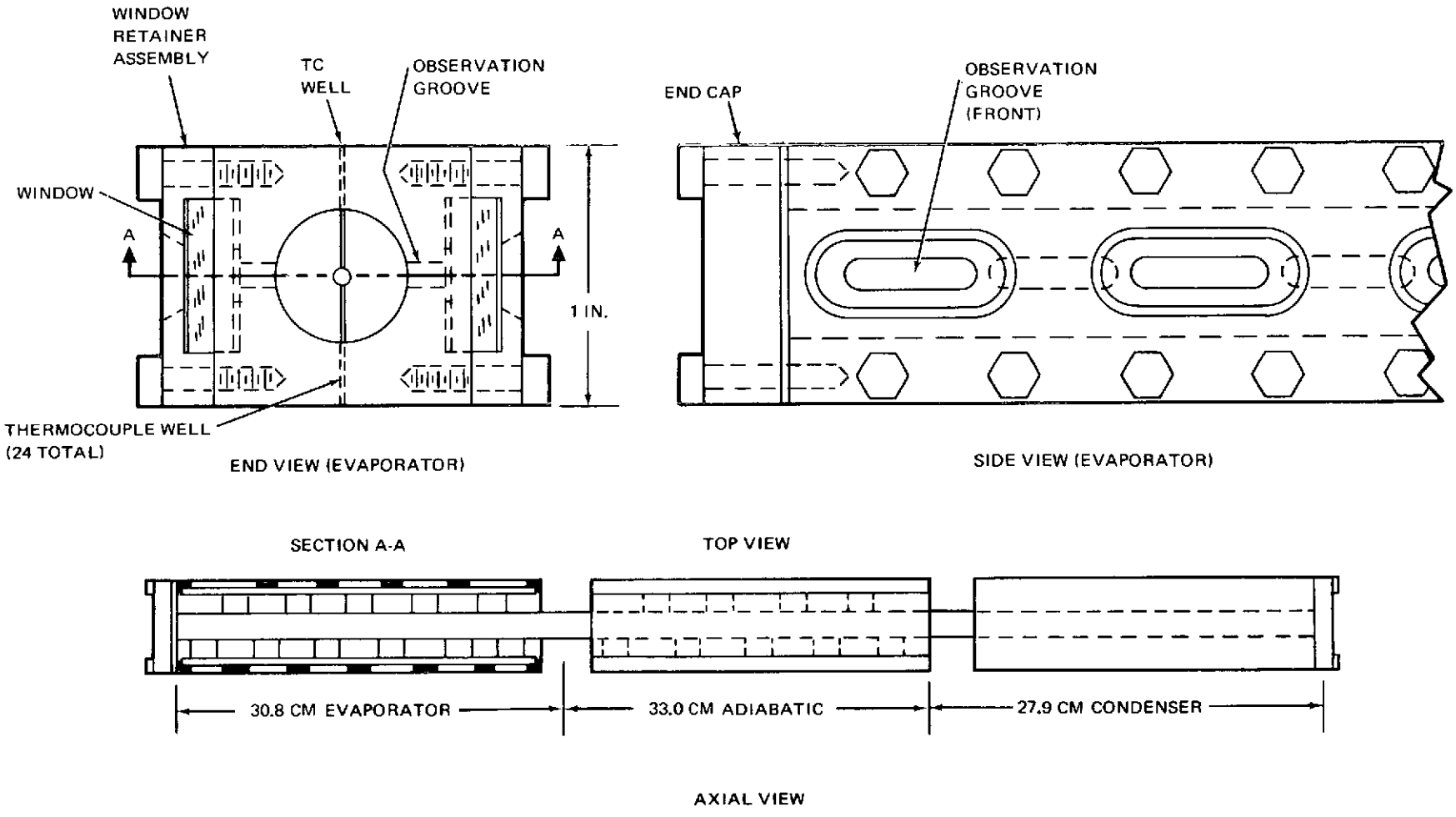

Figure 3-1. Heat Pipe with Observation Ports

Table 3-1

PORTED HEAT PIPE SPECIFICATIONS

Over Dimensions	2.03 cm wide x 2.54 cm high x 91.7 cm long
Evaporator Length	30.80 cm
Adiabatic length	32.96 cm
Condenser Length	27.94 cm
Inside Diameter	1.27 cm
Wicking	0.159 cm ID artery on axis. Artery and web 2 and 4 layers of 200 mesh stainless-steel square-weave screen, respectively. Wall wick 1 layer of 200-mesh screen.
Observation Ports	22 slit ports, evaporator and adiabatic
Port length	2.54 cm
Width	0.246 cm Optical glass against Buna-N O-rings
Working Range:	
Temperature	-20°C to 100°C
Pressure	Vacuum to 200 psig
Thermal Insulation	0.343 w/°K (based on sum of evaporator and adiabatic length)
Condenser/Film Heat Transfer Coefficient*:	
Methanol	0.102 $w/cm^2/°K$
Ammonia	0.224 $w/cm^2/°K$

*Referenced to entire inside circumference; condenser thermocouples on centerline of top face.

3.2 EXPERIMENTAL TECHNIQUES

3.2.1 Heat Pipe and Fluid Processing

Prior to all heat pipe testing, the working fluid was degassed in a reflux distillation column, and the heat pipe was evacuated to approximately 10 microns. Gas chromatographic analysis indicates principal impurities in the anhydrous ammonia were about 100 ppm of N_2 and 30 ppm of H_2O. Methanol used was Baker-certified spectrometric quality. With liquid in the heat pipe and a 10-w thermal load, vapor venting at the condenser eliminated any gases by vapor flow scavenging. Because in-situ venting results in the cleanest system, the pipe was heavily overloaded initially, and sufficient vapor was bled off through the venting cycles to yield a nominally primed arterial structure with no significant pool at the bottom of the pipe. The heat pipe was operated with an overall adverse fluid head, although the head varied slightly along the pipe because of permanent orientations each section assumed on welding. Relative heights are given in Table 3-2, using the far condenser end as reference. Although the heat pipe load was determined primarily by visual observation, post-test weight measurements of fluid place the average ammonia load at 15 grams and the average methanol load at 16.5 grams. Over the temperature ranges used, nominal calculated loads are 10.7 grams and 11.9 grams, respectively, accounting for fluid needed to fully saturate screens, prime the artery, develop menisci at the arterial stem base, and form fillets within the observation ports. Excess fluid was distributed within the arterial stem fillets and as a small puddle at the far end of the condenser.

Excess fluid also collected under the arterial foot. When the artery was pulled into the heat pipe, pressure contact at the base of each stem forced the stem foot into a half-moon shape and created a v-shaped cavity at the juncture of the foot and wall. Both the fillets and cavity served to store liquid and provide an alternate condensate return path. The effect of these alternate paths was very apparent in experimental testing.

3.2.2 Trace-Gas Experimental Tests

Two separate test sequences were used to characterize occlusion behavior in an operating heat pipe. In the first test series, degassed working fluid

Table 3-2
HEAT PIPE ELEVATIONS DURING TESTING

Position	Elevation (cm)
Condenser Blind End	0.00
Condenser Center	0.06
Condenser/Adiabatic Transition	0.12
Adiabatic/Evaporator Transition	0.08
Evaporator Blind End	0.15

was loaded into the evacuated heat pipe, and vapor purges were used to scavenge trace gases and attain the operating fluid load. The number of purges were typically between 5 and 10, and were performed in about one hour. At this point, the system was in the most- gas-free condition possible, and any remaining gases can normally not be removed by standard fluid processing techniques.

The effects of residual gases were determined both statically and dynamically. That is, for a static test, the heat pipe was elevated to 30.5 cm for two minutes to completely deprime the artery. The heat pipe was then returned to horizontal, and occlusion collapse recorded as a function of time. In the dynamic test, the heat pipe was elevated, deprimed, returned to horizontal, the evaporator heater was energized, and behavior of the occlusion was recorded as a function of input power. Dynamic and static tests were performed at two different temperatures to establish temperature dependence. Dynamic trace gas tests are discussed with dynamic gas additive tests for continuity.

3.2.3 Gas-Additive Experimental Tests

Initially, a small collapsing trace-gas occlusion was generated in the evaporator. When occlusion length was about 0.05 to 0.10 of the heat pipe length, occlusion behavior was observed as noncondensable gas was introduced into the condenser. Gas introduction was terminated when one-half the condenser had a depressed temperature, indicating gas presence. Table 3-3 summarizes average gas loadings for each test. Heat transport rate was then increased until occlusion length stabilized, then input power was increased to a maximum level of

Table 3-3

NOMINAL GAS CHARGES FOR GAS-ADDITIVE TESTS

Fluid	Gas	T_1(-15°C) (cm^3 at STP)	T_2 (10°C) (cm^3 at STP)	T_3 (15°C) (cm^3 at STP)	T_4 (30°C) (cm^3 at STP)
Ammonia	He	7.7	11.7		
	Ar	7.7	11.7		
	Xe	12.7	12.7		
Methanol	He			0.20	0.20
	Ar			0.20	0.20

70 watts, with occlusion length recorded at each power level. These tests demonstrated the effect, or lack of an effect, of a noncondensable gas zone on occlusion stability in terms of dissolved gas in return condensate and subcooling effects. The gases helium and argon were used with methanol at two temperatures; the gases helium, argon, and xenon with ammonia at two temperatures.

3.3 TEST RESULTS/TRACE GAS EFFECTS

Figures 3-2, 3-3, and 3-4 present representative experimental data on quasi-static collapse rates for trace gas occlusions in ammonia and methanol at two temperatures. The occlusions collapse with a half-life of 10 to 300 sec, depending on the amount of noncondensable gas that enters the artery on depriming. Observations over longer periods show the total time to collapse is on the order of 30 to 60 min maximum. These experiments are quasi-static because, at the test temperatures of -15°C and 10°C, parasitic heat loads of about 10 and 2 watts were taken in through adiabatic and evaporator insulation packages. The test results reflect occlusion collapse in the presence of modest fluid transport rates, except for tests conducted at 15°C laboratory ambient.

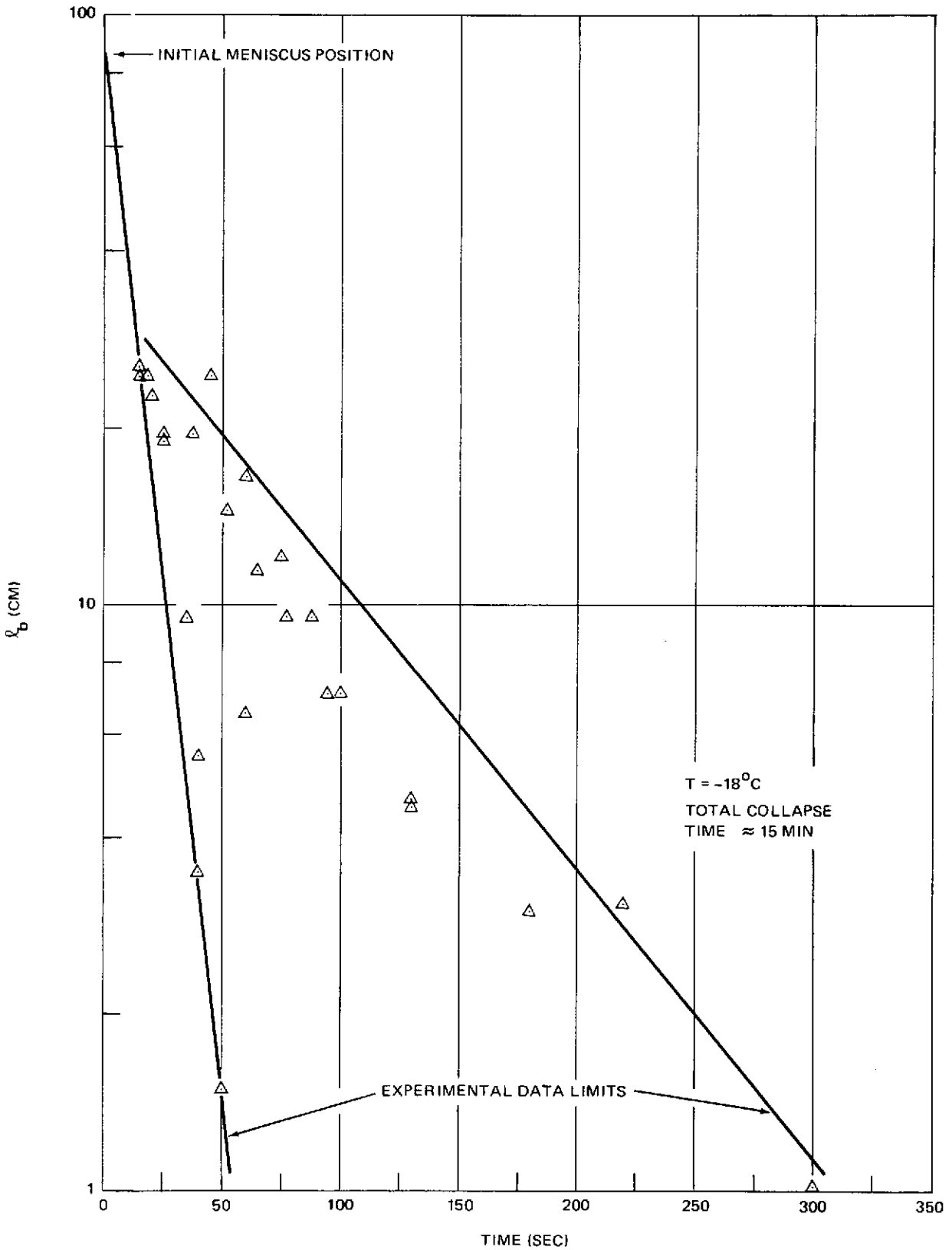

Figure 3-2. Occlusion Collapse in Degassed Ammonia at -12.5°C

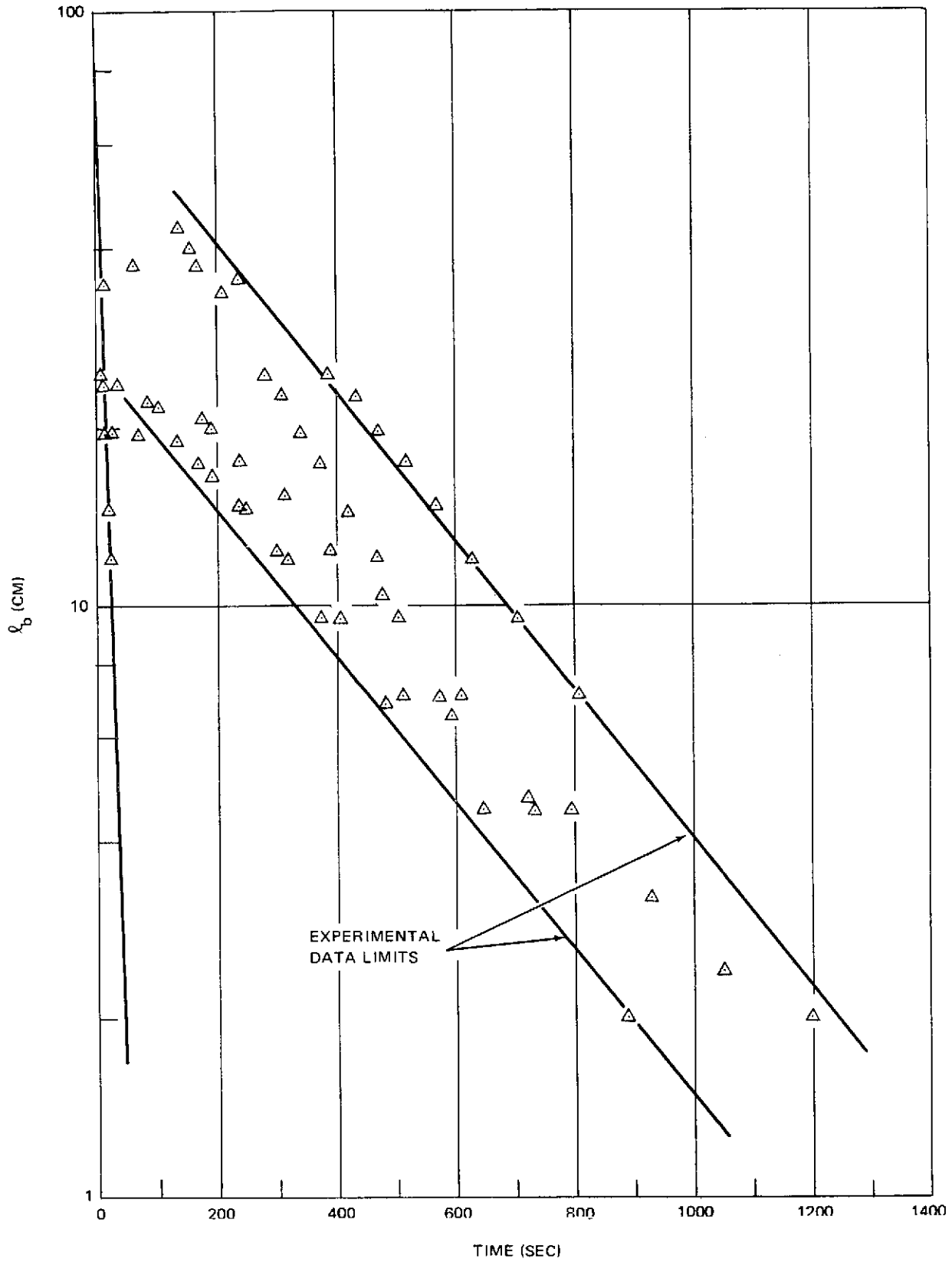

Figure 3-3. Occlusion Collapse in Degassed Ammonia at 10°C

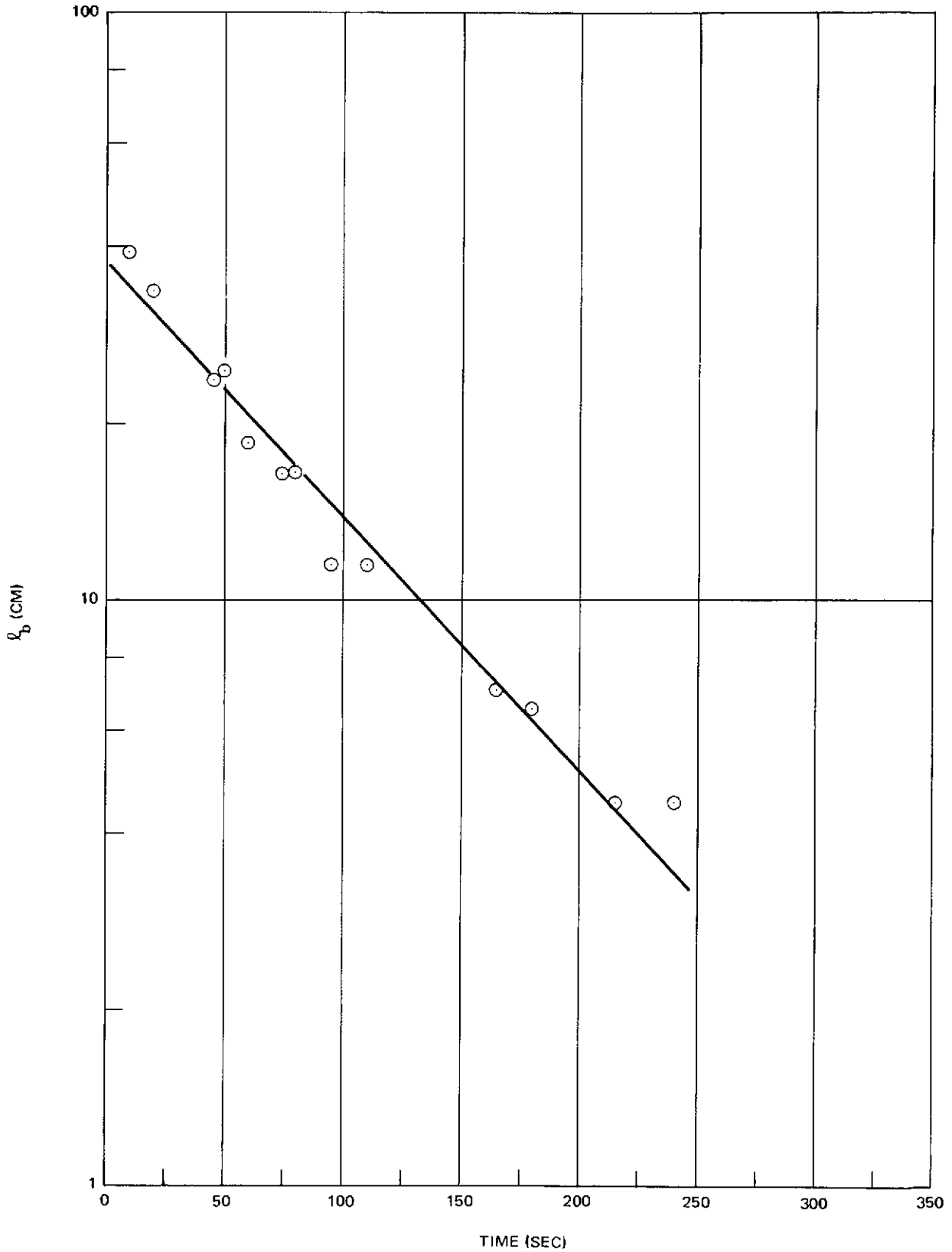

Figure 3-4. Occlusion Collapse in Degassed Methanol at $10^{o}C$

Because collapse rates are slow, estimates were made of the noncondensable gas level remaining in the heat pipe. As shown in Figures 3-2, 3-3, and 3-4, the occlusion initially collapses rapidly until the occlusion internal gas pressure is balanced by the surface tension driving pressure. Beyond this point, the occlusion collapses as the result of gaseous diffusion through the arterial envelope. As discussed in Reference 2, the differential equation describing diffusion collapse predicts an exponential time dependence, and data support this conclusion. At the initiation of diffusional collapse, the pressure equilibrium is

$$P_{g\gamma} \cong \frac{2\gamma}{r_a} - \rho g h - \Delta P_{cl} \qquad P_{g\gamma} > 0 \qquad (1)$$

For a parasitic heat load of 2 watts at 10°C, ΔP_{cl} can be neglected. In the tilted and deprimed condition, the internal arterial gas pressure should reflect the order of magnitude of impurity gas within the heat pipe vapor. The partial pressure of gas can be estimated as

$$P_{gv} \sim \frac{P_{g\gamma} \ell_b}{\ell_c + \ell_a + \ell_e} \qquad (2)$$

With these assumptions, the partial pressures of gas in ammonia and methanol are on the order of 100 and 12 microns. In the vapor phase, the relative impurity levels at 10°C are 23 and 250 ppm, and if the principal impurity is assumed to be nitrogen, equilibrium liquid impurity levels are 0.015 and 0.004 ppm, respectively.

The 100-microns gas partial pressure in ammonia is not indicated in any way by a colder gas zone, to the limit of digital equipment used (0.1°C). The 12-micron estimated gas partial pressure in methanol may produce a small gas leg (~1 cm) at power levels of 2 to 10 watts with a 0.1° to 0.2°C overall gradient. A slow gas build-up over several hours was observed with methanol and it may result from the large number of O-rings which allow diffusion of air into the experiment. However, methanol collapse rates reflect data taken immediately after vapor purging.

Reference 2 presents an expression for calculating the half-life of elongated occlusions as

$$\tau_{1/2} = \frac{0.693\ r_a^2\ \ell n\left(1 + \frac{\delta}{r_a}\right)}{2\alpha D' (1-F)} \qquad (3)$$

where δ is the artery envelope thickness, D' is the effective gas/fluid diffusion coefficient, and (1-F) is the concentration gradient factor. From Figures 3-3 and 3-4, half-lives of 240 and 70 sec are representative of collapse rates following the initial rapid length change. The effective diffusion coefficient for an arterial wall of 2 layers of 200-mesh screen is about 0.425 $D_{g\ell}$ (Reference 2). At 10°C, the heat pipe is transporting about 2 watts of parasitic input; if the modeling of Section 2 is correct, the gas content in the evaporator vapor space should be low because of sweeping action, and the concentration factor should be close to 1.0. On the other hand, if the vapor phase has an axially uniform gas content, then the rapid occlusion shrinkage to half the artery length implies $(1-F) \sim 1/2$. Using both assumptions, Table 3-4 presents a comparison of calculated values of the fluid property factor $\frac{1}{\alpha D_{g\ell}}$ with values obtained experimentally (Reference 2) for argon and helium. Nitrogen is the most probable impurity in both the ammonia and methanol experiments, and has properties intermediate to argon and helium.

The calculated venting parameter, $\frac{1}{\alpha D_{g\ell}}$, is closest to the experimental values when (1-F) = 1.0 for methanol, and (1-F) = 1/2 for ammonia. Although order-of-magnitude agreement for the simple model is obtained without making this distinction, adjustment of the diffusion factor may have a physical basis. The vapor density of ammonia is about 100 times the vapor density of methanol at 10°C, and therefore, the vapor Reynolds numbers are inversely related, creating much more vigorous sweeping action with methanol than with ammonia at this temperature. The presence of this vapor-related effect is also indicated by the collapse data taken at -15°C with ammonia (Figure 3-2). At -15°C, the vapor pressure of ammonia is only 2.3 atmospheres, and the implied venting parameter is approximately 44,000 sec/cm^2 if (1-F) = 1.0. The experimentally measured values for argon and helium are 70,000 and 400,000 sec/cm^2. Therefore, at a lower vapor pressure, the more theoretically satisfying choice (1-F) = 1.0 is justified by experimental data.

In general, the calculated values of $1/\alpha D_{g\ell}$ are low for these quasi-stagnant tests even in the case of a sufficiently high vapor flow Reynolds number. This results in part from fluid flow in the arterial envelope causing some radial mass convection, which augments diffusion, and causes D' to increase.

Table 3-4

COLLAPSE RATE CORRELATION OF VENTING PARAMETER $\frac{1}{D_{g\ell}}$ AT 10°C

Fluid	Experimental Venting Parameter		Implied Value	Implied Value
	Argon (sec/cm^2)	Helium (sec/cm^2)	(1-F) = 1 (sec/cm^2)	(1-F) = 1/2 (sec/cm^2)
Ammonia	33, 100*	275, 000*	211, 000	106, 000
Methanol	75, 000	200, 000	61, 000	30, 500

*Values extrapolated from low temperature data in Reference 2.

Accepting some error from uncertainty in the factor $(1-F)D'$, agreement is adequate that collapse rates at low power levels can be estimated by Equation 3. An adequately low power level is defined such that the condensate is not supersaturated with gas, and $P_{g\gamma}$ is positive and non-negligible. The factor (1-F) is

$$1-F = \frac{P_{g\gamma}}{P_\infty + P_{g\gamma}} , \qquad (4)$$

where P_∞ is the general vapor phase gas partial pressure at the outside envelope of the artery.

3.4 GAS ADDITIVE TESTS

Figures 3-5 through 3-8 show the effect of heat transfer on occlusion stability for the working fluids ammonia and methanol with gas addition as described in Section 3.2.3. Occlusion response to power is also shown for degassed working fluid.

To power levels from 10 to 20 watts, heat transfer does not materially reduce the capability of an ammonia occlusion to collapse with the secondary wicking and fillets present in these experiments. For methanol, a similar limit to approximately 5 watts is shown. Beyond this range, the occlusion lengthens with power increase and stabilizes at a new length. The small length change for an ammonia occlusion at low power is not completely understood. This behavior is partly attributable to the non-uniform elevations of Table 3-2,

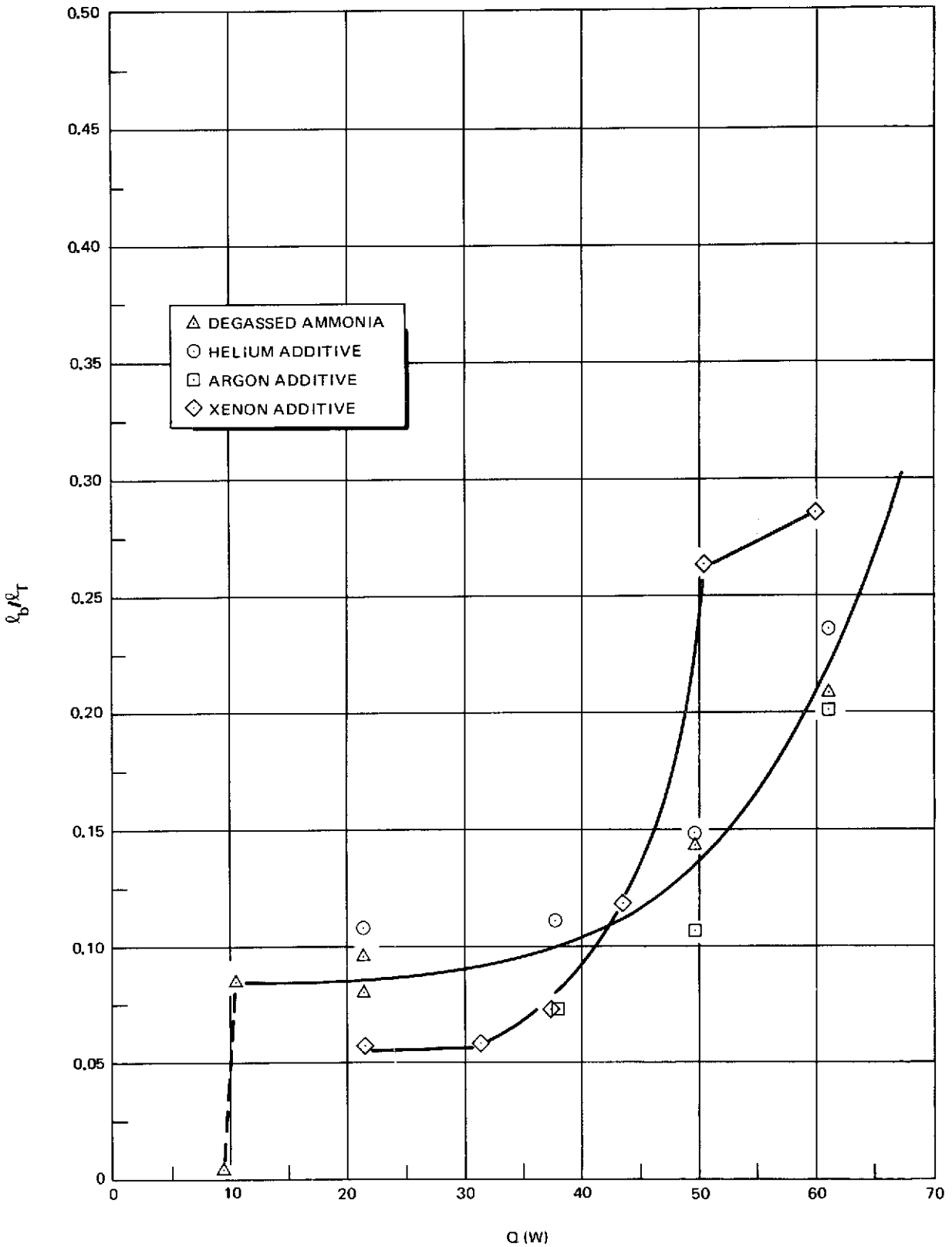

Figure 3-5. Arterial Depriming with Heat Transfer for Ammonia at -15°C

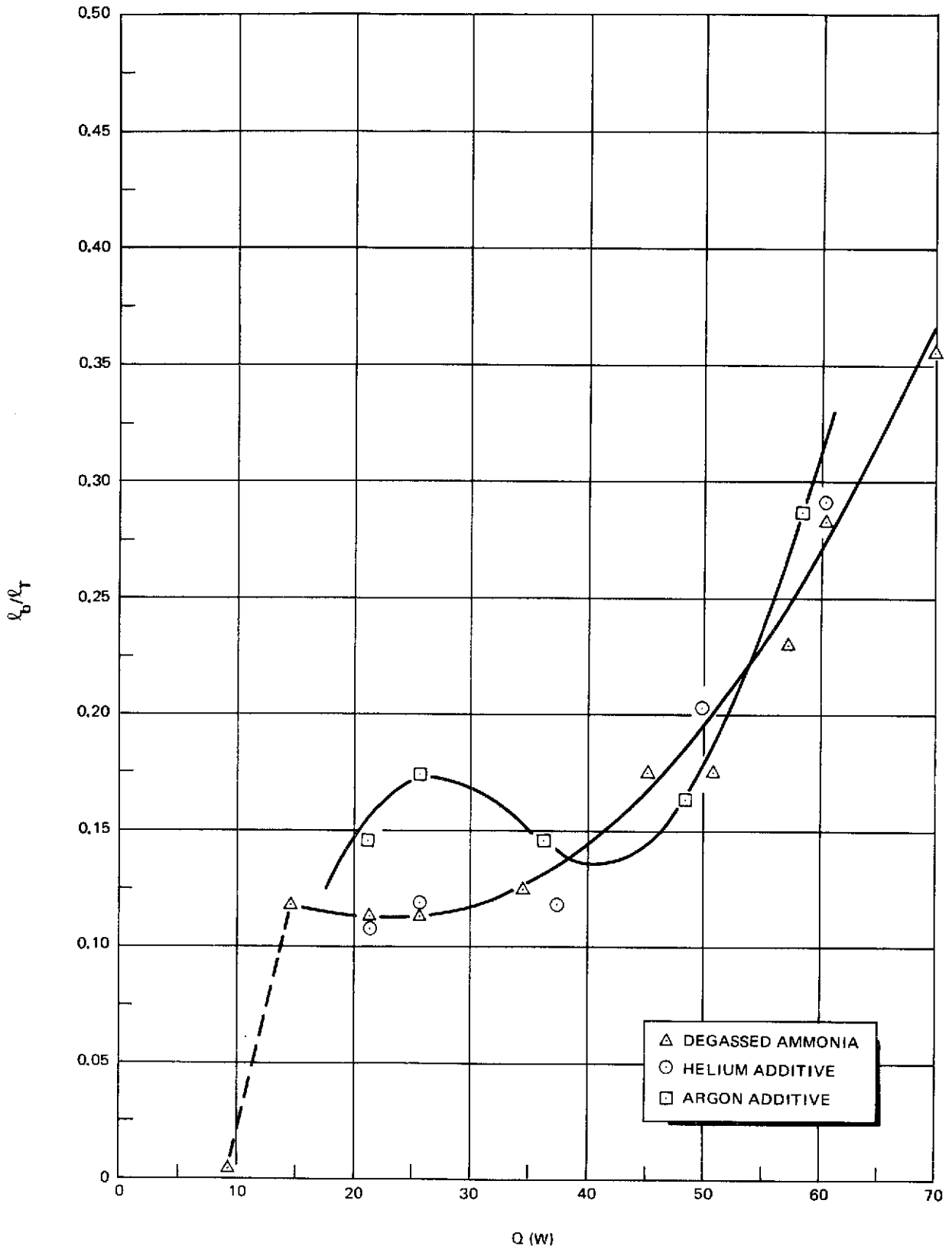

Figure 3-6. Arterial Depriming with Heat Transfer for Ammonia at 10°C

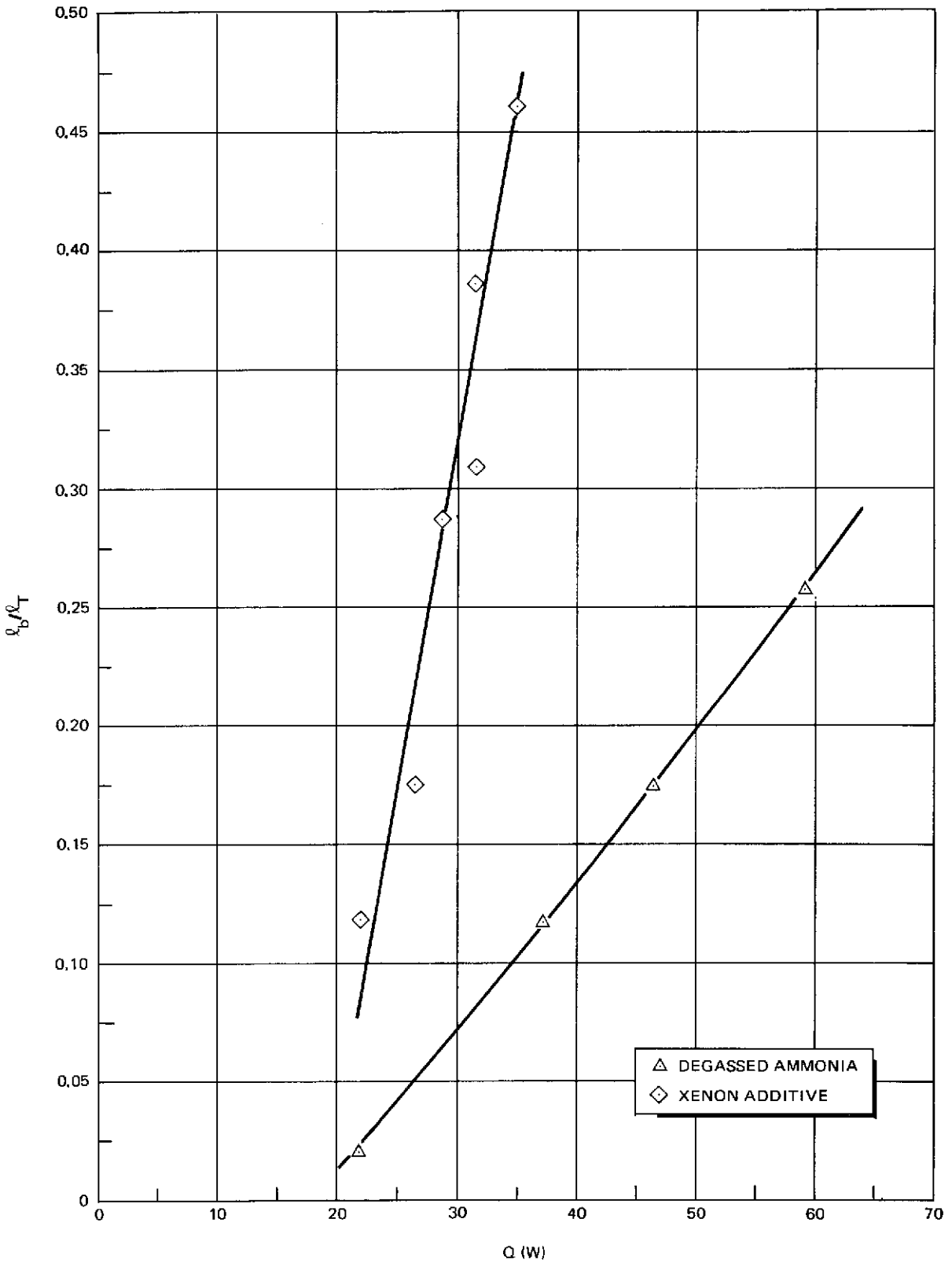

Figure 3-7. Anomalous Arterial Depriming for Xenon in Ammonia at $10^{o}C$

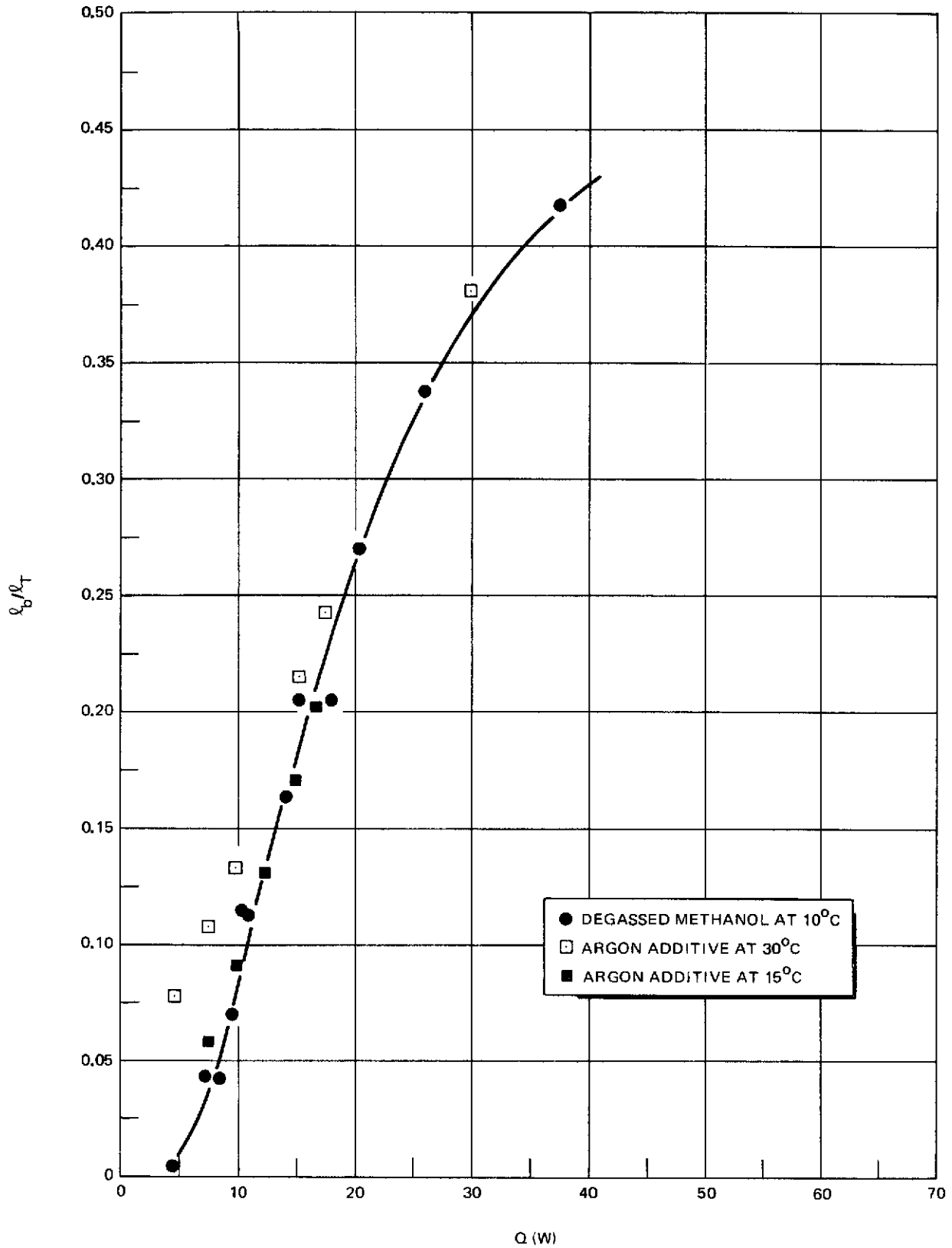

Figure 3-8. Arterial Depriming with Heat Transfer for Methanol at 15°C

coupled with the fluid overload. Helium and argon in the condenser do not materially alter occlusion growth rates with power, while xenon very significantly increases sensitivity to power increase. As discussed in Section 2, gases with low diffusion coefficients, such as zenon, are carried further distances with condensate than high diffusivity gases such as helium. Argon is intermediate in behavior. These transported gases then evolve into the occlusion, lengthening it as described by equations in Section 2. However, the following sections show that the absolute quantity of gas transported should have been negligible in all cases, and xenon behavior is anomalous. Xenon gas profiles in R-22 tests described in Appendix A were also anomalous.

3.5 INTERPRETATION OF EXPERIMENTAL DATA

In Section 2, a model was derived for diffusive loss of gas from tube-flow. Applied to a heat pipe artery, this expression is equivalently given as

$$P_{g2} = \tilde{P}_{gc} \left(\frac{\tilde{z}}{z_o + \tilde{z}}\right) \text{EXP}\left(-\frac{11.35\,\rho D_{g\ell} h_{fg} z}{M Q_a}\right) \tag{5}$$

where P_{g2} is the equilibrium gas partial pressure at the occlusion, P_{gc} is the partial pressure of gas in the condenser over the zone of mixed condensation, and Q_a is the heat-equivalent fluid transferred by the artery, subtracting from the gross transfer rate all heat transferred by secondary wicking. This equation will be used to show that dissolved gases were almost completely lost in the experiments discussed. In Equation 5, z is the distance between the gas uptake zone and occlusion head. Because most of the data show no effect of trace gases or gas additives, these data were correlated with the simple model

$$\Delta P_{c1} = \frac{2\gamma}{r_a} - \rho g h \tag{6}$$

Figures 3-9 and 3-10 present data correlation on this basis. For both ammonia and methanol, the fluid conductance of the secondary wicking is indicated to be 5 to 10 times that of the artery. Independent calculations substantiate that the stem fillets and pool, transfer fluid to the occlusion head at about the implied rates. This fluid shunting has a significant effect on gas transport.

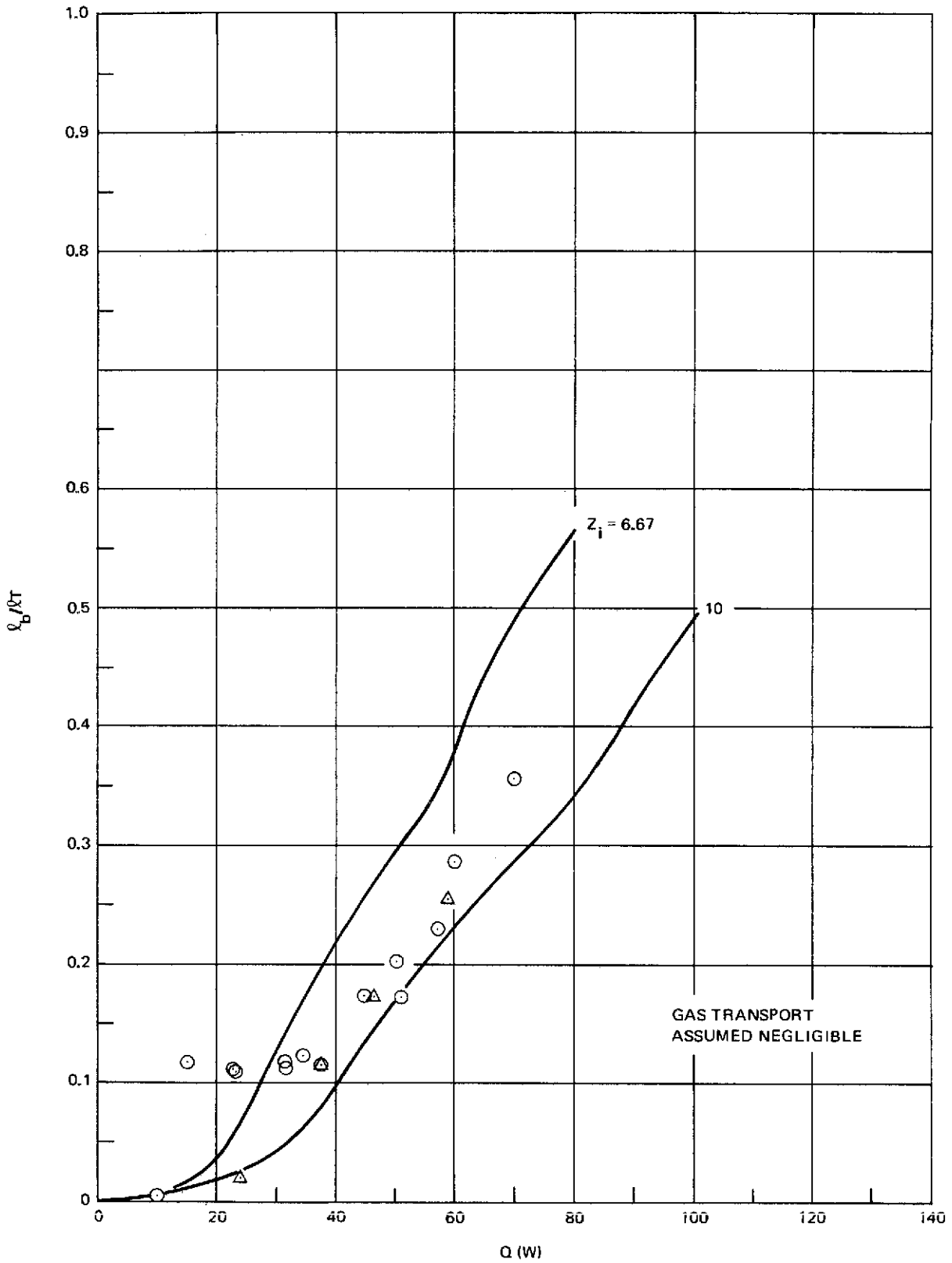

Figure 3-9. Comparison of Arterial Depriming with Theory for Ammonia at 10°C

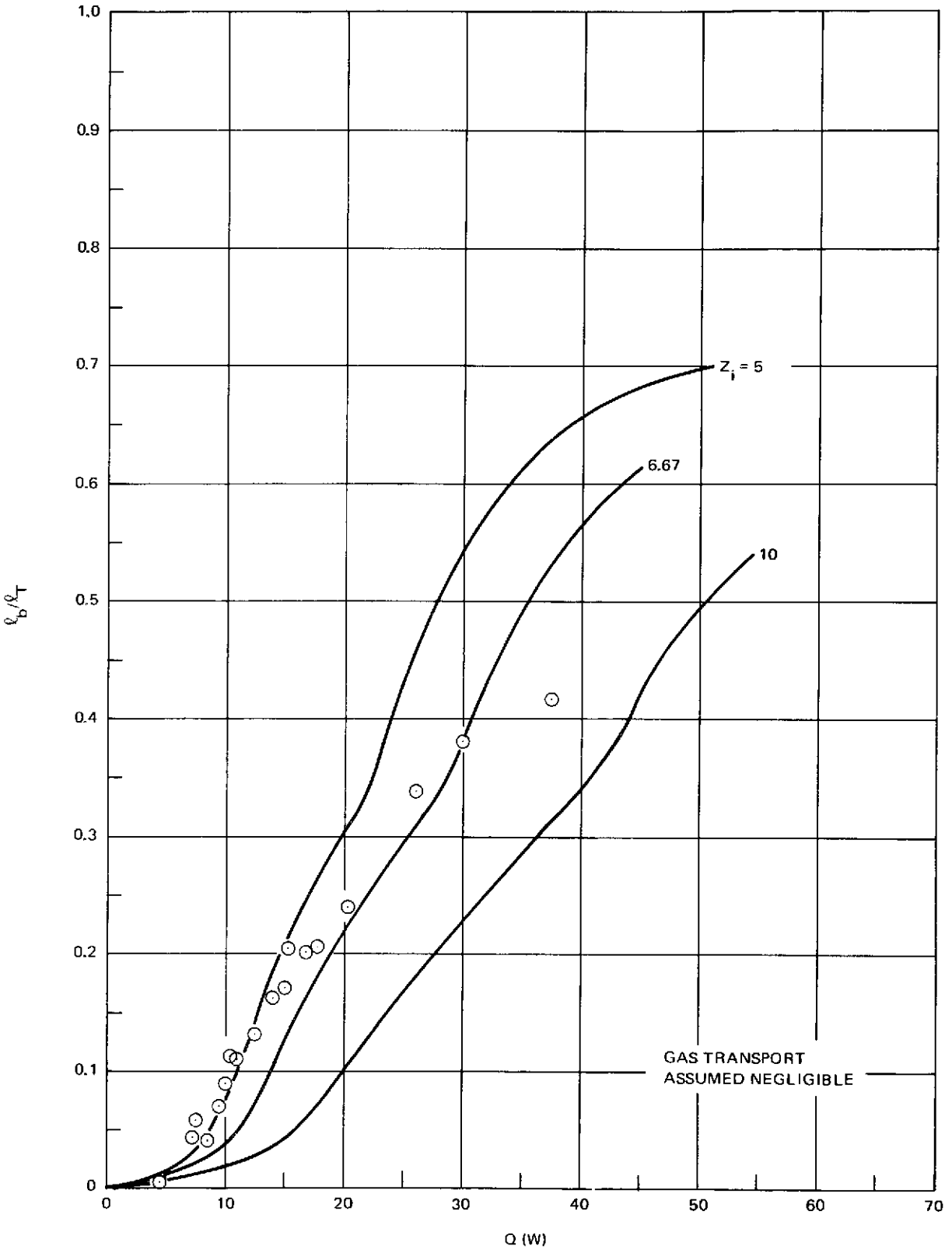

Figure 3-10. Comparison of Arterial Depriming with Theory for Methanol at 15°C

In Equation 5, Q_a is on the order of 0.125 Q_{TOT}. Substituting experimental values for the factors in 3.5 (Reference 2), the gas pressure P_{g2} at 10° to 15°C is

$$P_{g2} \sim 522 \text{ EXP}(- c_i z/Q_{TOT}) \quad \text{(methanol)} \quad (7)$$

$$P_{g2} \sim 17,000 \text{ EXP}(-c_i z/Q_{TOT}) \quad \text{(ammonia)} \quad (8)$$

The interfacial conductance G_i has been taken to be 0.57 w/cm/°K, and the average condenser partial gas pressure has been taken to be 25% of the maximum partial pressure. The maximum condenser gas leg ΔT was on the order of 3° to 5°C. The coefficients c_i are

Methanol at 15°C:	He/Ar = 12.2/4.25
Ammonia at 10°C:	He/Ar/Xe = 11.6/16.8/3.94

For P_{g2} to be relevant, it must be on the order of 10% of 2 γ/r_a. For z on the order of 80 cm, as typical of this experiment, the maximum value of P_{g2} (Xe) is about 0.5 dyne/cm^2 at 30 watts, and 89 dynes/cm^2 at 60 watts. The factor 2 γ/r_a is about 500 dynes/cm^2. Therefore, in all cases, at low power, the effects of gas dissolution should be small. This was observed for all combinations, with the exception of xenon, and possibly argon, at 10°C (Figure 3-6).

The unusual behavior of argon and xenon appears to be related to the high solubility of these two gases in the working fluid, together with a pressure-dependent phenomena discussed in Section 3.3. The behavior of argon (Figure 3-6) could be interpreted as a vapor-phase effect where an increase in axial vapor velocity sweeps a stagnant gas layer away from the artery and allows gases within the condensate and occlusion to escape to the vapor phase.

Where gases are not completely lost in transit to the occlusion, the expression for occlusion length derived in Appendix B is applicable under conditions where assumptions are valid. Utilizing expressions of Section 2 for gas transport and occlusion internal pressure, ℓ_b is given as

$$\ell_b = \frac{\bar{v}\delta^2}{2D'} \left[\frac{0.818\, P_{gc} \left(\frac{\bar{z}}{z_o+\bar{z}}\right) \mathrm{EXP}\left(-11.35 \rho D_{g\ell} h_{fg} z/M\Omega_a\right)}{\frac{2\gamma}{r_a} - \rho g h - \Delta P_{cl}} - \frac{2}{3} \right] \quad (9)$$

As discussed in Section 2 in relation to g*, gas solubility does not appear explicitly in this occlusion stability criteria. This model was not compared to experimental data because of uncertainty in estimating the flow velocity $\bar{v}$ for the experimental system used. In addition, gas transport effects have been shown to be small, in agreement with the order-of-magnitude argument developed.

Section 4
CONCLUSIONS

In a previous investigation (Reference 2), the stability of an occlusion in a static heat pipe was characterized. As long as the following occurs, an occlusion collapses, even if slowly.

$$\frac{2\gamma}{r_a} \geq \rho g h$$

The collapse rate depends inversely on the artery diameter squared and the internal partial pressure of gas, and directly on the solubility-diffusivity product, $\alpha D_{g\ell}$. In a dynamic system, the corresponding stability criteria are

$$\frac{2\gamma}{r_a} \geq \rho g h + \Delta P_{cl}$$

$$\int_o^{\ell_b} \frac{\partial c_{g\ell}}{\partial r} \, dz \leq 0$$

The first is a simple hydrodynamic pressure constraint. The second requires the integrated flux of gas into the occlusion to be either zero or negative, i.e., the occlusion cannow grow with time. Expressions have been developed which predict whether the second criterion is met. In general, these expressions, (e.g., Section 2, Equations 9 through 13) depend on many factors because the occlusion is now in mass communication with the condenser, and the entire heat pipe environment. Maximum diffusivity is still desirable. In all cases, however, the criteria do not have solubility as an explicit factor. Although collapse rate is still proportional to solubility (Section 3, Equation 3), a high solubility is not required for diffusional collapse. Indeed, in dynamic systems, high solubility gases have exhibited very peculiar behavior.

Within the limit of highly soluble gases such as xenon, and in some cases argon, the well-defined gas zone within a gas-loaded heat pipe spreads so that the return condensate is significantly enriched with dissolved gas and occlusions

are extremely unstable. In addition, conflicts between experimental data and analysis indicate that, for high pressure fluids, significant gas gradients at low power occur within the vapor core surrounding the artery. These gradients retard gas loss by the artery and therefore accentuate occlusion problems. With low solubility gases such as helium, the presence of significant amounts of gas in the condenser does not affect occlusion stability. Occlusion stability in these cases is dominated by hydrodynamic pressure drops. At low power levels, occlusions will collapse. Above a critical power level, occlusions systematically lengthen in response to heat input until secondary wicking cannot sustain the fluid pressure drop and the heat pipe burns out. In general, there are no fundamental improvements in gas occlusion resistance in the dynamic system. Condensate subcooling by condenser function is not adequate to collapse occlusions, and fluid flow around the occlusion, which augments diffusion, occurs at the expense of a large hydrodynamic pressure drop.

Several options are possible which individually or collectively can reduce failures of high performance heat pipes from arterial malfunction. Several are already being investigated.

First, it appears possible that forced cooling of condensate can significantly accelerate the loss of noncondensable gas by compressing the gas via the Clapeyron effect. By suitable arterial design, it also may be possible to force the gases to vent through the arterial skin. By leaving the arterial ends open and increasing artery diameter, high gas-resistance can be achieved in a high performance pipe. However, the larger diameter generally precludes 1-g testing. By forming many arteries into a bundle, high redundancy can be achieved along with some subcooling. By using large axial grooves, or electrostatic fluid pumping, fluid structures with open faces which will not form occlusions can be used. Finally, most arterial systems benefit from a warm-up period at a low power such that noncondensable gases are segregated to the condenser and the artery can expel gas by simple diffusion.

Section 5
SYMBOLS

A_s	secondary wicking cross-section, cm^2
A_w	wall cross-sectional area, cm^2
A_v	vapor core cross-sectional area, cm^2
C	total vapor concentration, g-moles/cm^3
$C_{g\ell}$	initial gas concentration in condensate, g-moles/cm^3
C_{g1}	induced gas concentration in liquid, g-moles/cm^3
C_{g2}	gas concentration in liquid due to transport, g-moles/cm^3
C_p	specific heat, joules/gm/°K
D_{ab}	vapor phase binary diffusion coefficient, cm^2/sec
$D_{g\ell}$	diffusion coefficient for gas in liquid, cm^2/sec
f	dimensionless gas pressure
f_c	sub-cooling enhancement factor
G	per-unit-length conductance, w/cm/°K (subscript f = fluid film, i = wall/jacket interfacial conductance, j = jacket/coolant interfacial conductance)
h_{fg}	latent heat of vaporization, joules/g-mole
K_h	Henry's Law constant, dynes/cm^2
K_ℓ	liquid thermal conductivity, w/cm/°K
K_{ps}	permeability of secondary wicking, cm^2
K_w	wall thermal conductivity
ℓ_a	adiabatic length, cm
ℓ_b	occlusion length, cm
ℓ_c	condenser length, cm
ℓ_b	occlusion length, cm
ℓ_e	evaporator length, cm
ℓ_o	initial occlusion length, cm
M	fluid molecular weight, gms/g-mole
$\dot{n}_v$	vapor flow rate, g-moles/sec
$\dot{n}_g$	gas flow rate, g-moles/sec
P_a	total heat pipe internal pressure, dynes/cm^2

P_b	occlusion total internal pressure, dynes/cm^2
P_c	critical point vapor pressure, dynes/cm^2
P_g	gas partial pressure, dynes/cm^2
P_{gl}	gas partial pressure after occlusion expansion, dynes/cm^2
P_r	reduced vapor pressure, P_{vs}/P_c
P_{vs}	vapor core saturation vapor pressure, dynes/cm^2
P'	temperature derivative of vapor pressure, dynes/cm^2/°K
Q	heat transfer rate, watts
Q_ℓ	$G_f \Delta T^*_{vw}$, w/cm
Q_m	maximum heat transfer rate, by artery alone, watts
q_c	local condensation rate, watts/cm
q_{co}	condensation rate with no end effects, watts/cm
r_a	artery radius, cm
r_c	critical capillary radius, cm
R	gas constant
T	temperature, °K (subscripts v = vapor, w = wall, j = condenser jacket, c = reference sink temperature)
T^*	$(T - T_c)/(T_a - T_c)$
T^*_{wl}	wall temperature at $z = z_o$
T_{cr}	critical temperature, °K
T_r	reduced temperature, T/T_c
T_{vs}	vapor temperature equivalent to P_{vs}, °K
T_{zm}	wall temperature at $z = z_m$, °K
V_m	centerline fluid velocity
X_g	mole fraction noncondensable gas in vapor phase
$X_{g\ell}$	mole fraction noncondensable gas in liquid phase
z	axial measure, cm
z'	fin factor describing vapor temperature profile, cm
$\bar{z}$	fin factor, $\sqrt{A_w K_w / G_i}$, cm
z_m	total condenser length, cm
z_o	gas zone boundary, cm
Z_i	permeability-area product of secondary wicking divided by product for primary wicking
z^*	dimensionless axial distance, $z^* = z/\bar{z}$
z^*_{ow}	$z_o/\bar{z}$
z_r	z/z_m

α	Ostwald coefficient
β	G_i/G_f
γ_s	fluid surface tension, dynes/cm
ΔP	pressure difference, dynes/cm^2
ΔT^*_{vw}	dimensionless temperature difference at $z = z_o$
ζ	ratio of gas partial pressure to system pressure in a static heat pipe
$\eta_{h,m}$	thermal or mass loss factor for tube-flow
$\theta_{h,m}$	thermal and mass diffusion coefficients, cm^2/sec
θ_a	advancing contact angle, radians
θ_e	equilibrium contact angle, radians
θ_r	receding contact angle, radians
λ	$\sqrt{1+\beta}$
μ	viscosity, poise
ε	$d(\ell n\, Pr)/d\, T_r$
ε'	$d\varepsilon/d\, T_r$
ρ	fluid density, g/cm^3
ϕ_a	molar flux of vapor, moles/cm^2/sec
ϕ_b	molar flux of gas, moles/cm^2/sec
$\psi_{c,a,b}$	fraction of heat pipe section with occlusion (subscript c = condenser, a = adiabatic, e = evaporator)

Section 6

REFERENCES

1. R. Kosson, et al. Development of a High Capacity Variable Conductance Heat Pipe, AIAA Thermophysics Conference, July 16, 1973.

2. E. W. Saaski. Investigation of Bubbles in Arterial Heat Pipes, NASA CR 114, 531, 1972.

3. A. M. Schwartz, et al. Resistance to Flow in Capillary Systems of Positive Contact Angle, from Contact Angle, Wettability, and Adhesion, American Chemical Society, 1964.

4. J. H. Hildebrand and J. M. Prausnitz. Regular and Related Solutions, Van Nostrand Reinhold Co., 1970.

5. B. D. Marcus. Theory and Design of Variable Conductance Heat Pipes, NASA Report CR-2018 (April 1972).

Appendix A
GAS PROFILE CHARACTERIZATION

The maximum amount of gas that can be dissolved in returning condensate is determined by interactions occurring in the diffuse frontal zone of the stagnant gas plug. In this region, condensation is occurring in the presence of noncondensable gas, and it can be assumed most gas is picked up in this region. The physical model developed at DWDL for characterizing heat and mass transfer in the gas-rich zone is shown in Figure A-1. A section of the heat pipe and heat rejection system is shown with a superimposed 4-level nodal system. In this multilevel one-dimensional model, the vapor temperature is assumed identical to the condensate film surface temperature. The wall is connected to the fluid/vapor interface and a cooling jacket through conductances G_f and G_i. The conductance G_i may be nonlinear if the coupling is by radiative transfer. Reflecting the model one-dimensionality, the interface conductances are effective total conductances per unit axial length; that is, the conductance is in units of watts/cm/°K. If the heat pipe is coupled to another heat pipe or a coolant loop, then a fourth level of nodes from T_j to T_c is required, with an interface conductance G_j.

Differential equations involving the position-dependent temperatures T_v, T_w, T_j, and T_c are derived. The algorithm for solving this non-linear equation system is given in Section A.3.

A.1 VAPOR PHASE MASS TRANSPORT EQUATIONS

Assuming a heat pipe of uniform cross-section, the transport equation will be solved for diffusive inviscid flow through a stagnant gas plug. That is, both axial and radial pressure gradients are neglected, and flow and temperature are assumed uniform across the cross-section. In terms of these model boundary conditions, the analysis is similar to that of Marcus (Reference A-1). However, certain simplifying assumptions used by Marcus have not been made here, and the mathematical approach is considerably different.

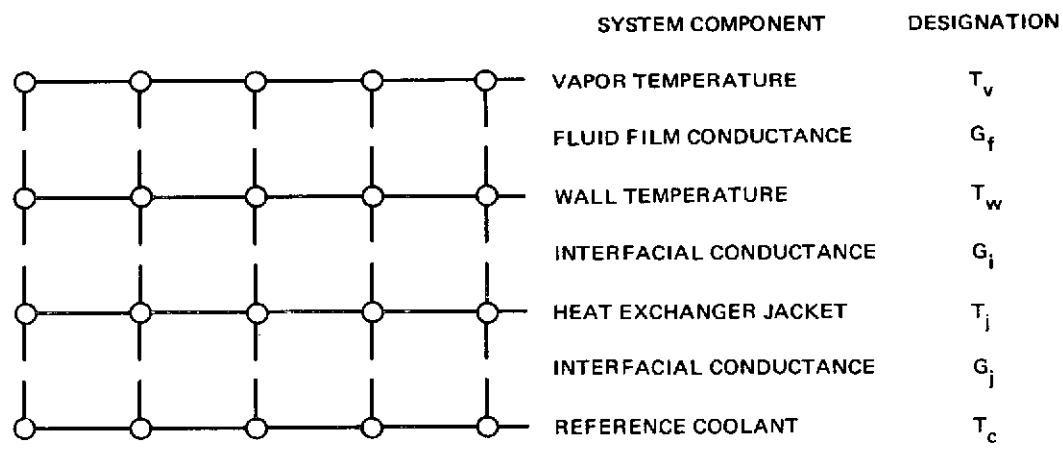

EQUIVALENT FINITE DIFFERENCE NODAL NETWORK

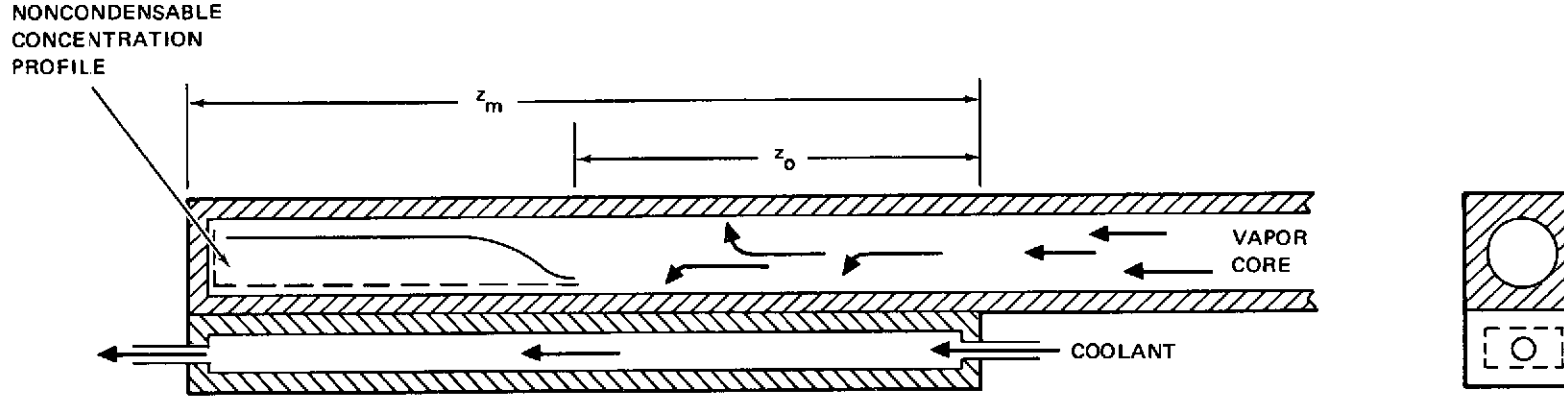

REPRESENTATIVE CONDENSER CONFIGURATION

Figure A-1. Finite Difference Representation for Gas-Loaded Heat Pipe

Conservation of working fluid vapor (denoted species A) at any cross-section results in the coupled mass-transfer/heat-transfer equation

$$\frac{d\phi_a}{d_z} = \frac{G_f (T_v - T_w)}{A_v h_{fg}} \tag{A-1}$$

where ϕ denotes molar flux and T_v and T_w represent the vapor and wall temperatures respectively. For uniaxial flow in which $\phi_b \equiv 0$ (b denotes insoluble, noncondensable gas); mass flux of species A is given as

$$\phi_a = \frac{C D_{ab} d X_a/dz}{(1 - X_a)} \tag{A-2}$$

so that

$$\frac{d}{dz} \left(\frac{C D_{ab} d X_a/dz}{1 - X_a} \right) = \frac{G_f (T_v - T_w)}{A_v h_{fg}} \tag{A-3}$$

It would be preferable to express the derivatives of mole fraction on the left-side in terms of T_v because a second-order equation in T_v is desired. This is entirely possible if the change of variable $U = \ell n (X_a)$ is made. Assuming the ideal gas law holds, then

$$U = \ell n(X_a) = \ell n(P_r) + \ell n \frac{P_c}{P_{vs}} \tag{A-4}$$

where P_r is the reduced vapor pressure at a given axial position and P_{vs} is vapor pressure in the heat pipe vapor core.

The first derivative of U with respect to z is expressible as

$$\frac{dU}{dz} = \frac{d}{dz} (\ell n P_r) = \frac{d(\ell n P_r)}{d T_r} \frac{d T_r}{dz} \tag{A-5}$$

where T_r is the local reduced temperature. The function U is defined in this manner to allow use of the Miller Correlation, a very accurate vapor pressure correlation given as (Reference A-2)

$$\ell n P_r = -2.303G'\left(\frac{1}{T_r} - T_r + g'\left(\frac{3}{T_r} + 1\right)\left(1 - T_r\right)^3\right) \tag{A-6}$$

where G' and g' are related to the critical temperature and pressure and the vapor pressure at the normal boiling point. Taking Equations (A-3) through (A-6), standard manipulations transform (A-3) into a differential equation in T_v.

$$\frac{d^2T_v^*}{dz^2} + \frac{T_a - T_c}{T_{cr}}\left(\frac{\varepsilon'}{\varepsilon} + \frac{\varepsilon}{1-X_a} + \frac{T_{cr}}{2T_v}\right)\left(\frac{dT_v^*}{dz}\right)^2$$

$$= \frac{T_{cr}G_f\left(T_v^* - T_w^*\right)}{A_v \varepsilon h_{fg} C D_{ab}}\left(\frac{1-X_a}{X_a}\right) \tag{A-7}$$

The dimensionless temperature T_v^* is defined in Section 5. The factor $T_{cr}/2T_v$ results from the derivative of $C D_{ab}$ with respect to z by assuming a Chapman-Enskog form for the factor, that is, $C D_{ab}$ is proportional to $\sqrt{T_v}$.

The nonlinear differential equation (A-7) relates vapor temperature to wall temperature T_w and axial position z.

A.2 DEFINITION OF AXIAL WALL CONDUCTION

The thermal conductivity of common fluid-saturated wicking materials is low relative to the thermal conductivity of typical heat pipe extrusions, and/or the cross-section of such wicking is small compared to the extrusion cross-section. For this reason, it is reasonable to assume that the fluid film acts primarily as an interfacial resistance and as a vapor pressure determining factor.

Assuming no radial or circumferential gradients within the heat pipe wall, a heat balance on a wall slice δz thick, as δz approaches zero, yields the differential equation

$$\frac{d^2 T_w^*}{d z_w^{*2}} = \left(1 + \frac{G_f}{G_i}\right) T_w^* - \frac{G_f}{G_i}\left(T_v^* - T_j^*\right) \tag{A-8}$$

For this development, the conductance G_i is assumed constant over the condenser length, although it is not a strict necessity.

An identical approach is used for the jacket cross-section, in the case of coupling to a coolant system.

$$\frac{d^2 T_w^*}{d z_j^{*2}} = \left(1 + \frac{G_j}{G_i}\right) T_j^* - T_w^* - \left(\frac{G_j}{G_i}\right) T_c^* \tag{A-9}$$

The equations described in this section, coupled with equation (A-7) completely describe the temperature profiles within the stagnant gas zone of a gas-loaded heat pipe.

A.3 NUMERICAL TECHNIQUES

Equations A-7, A-8, and A-9, describing the interaction of T_v, T_w, and T_j, respectively, are solved by applying the method of finite differences to the differential equations. A nodal system is set up as shown in Figure A-1, over both the gas-blocked zone and the freely condensing zone. The boundary conditions are

$$\frac{d T_v}{d z} = \frac{d T_w}{d z} = \frac{d T_j}{d z} = 0 \qquad \text{for } z = o \text{ and } z_m \tag{A-10}$$

$$\left.\frac{d T_w}{d z}\right|_{z = z_o^-} = \left.\frac{d T_w}{d z}\right|_{z = z_o^+} \quad ; \quad \left.\frac{d T_j}{d z}\right|_{z = z_o^-} = \left.\frac{d T_j}{d z}\right|_{z = z_o^+} \tag{A-11}$$

$$T_v = T_a \qquad z \le z_o \tag{A-12}$$

$$T_v = f\,(T_w, \phi_a) \qquad z > z_o \tag{A-13}$$

T_v, T_w, T_j continuous at $z = z_o$ (A-14)

The internal boundary z_o separates the gas-loaded zone beyond z_o from the freely condensing zone $0 \leq z \leq z_o$. At the interface $z = z_o$, Equations A-11 and A-14 specify continuity of axial heat flux and temperature.

Computational molecules used for the finite difference method are of the standard 2-point and 3-point types with respect to discretizing dT/dz and d^2T/dz^2. The 4-level system of coupled equations is solved by Gauss-Seidel iteration with successive over-relaxation (SOR).

Assuming irreducibility of the matrix system describing the nodal network, it can be shown that the SOR technique will converge to a true approximate solution of the differential equations if the temperatures $T_v(z)$ are continuously decreasing at all points from $z=z_o$ to $z=z_m$, when the Miller correlation is used as the analytic tie between T_v and the vapor pressure. The requirement of T_v continuously decreasing is physically consistent, and a numerical algorithm guaranteeing this condition is straightforward.

Other numerical techniques may be equally satisfactory to solve the system of differential equations. The SOR technique was chosen as a compromise between conservatism in stability and computational speed.

To calculate concentration and temperature profiles for a given charge of non-condensable gas, a value of z_o is estimated and an iterative solution of the equations is generated. The moles of gas are calculated as the integral

$$N = \int_{z_o}^{z_m} \frac{(P_a - P_v(z))\,dz}{R\,T_v(z)} \cdot \qquad \text{(A-14)}$$

The value of the integral is compared to the input moles, and a second estimate made for the proper value of z_o. The value of z_o is iterated until calculated gas content is within a small increment δ of the known moles of gas. The heat transferred is calculated as the integral over axial length of the radial heat transfer across the final conductance interface G_j.

A.4 MODEL COMPARISON/FEATURES

The one-dimensional model described in previous sections differs from the well-known model described by Marcus (Reference A-1). The primary difference is in not restricting the wall and fluid film temperatures to identical first and second derivatives. This allows the modeling of high-resistance condensate wicks as in heat pipes with low fluid conductivity, e.g., cryogenic heat pipes or organic fluid heat pipes. Without this restriction, it is necessary to solve the axial conduction problem in the freely-condensing zone as well. That is, the gas plug acts as a thermal sink and there is a very significant augmentation of the condensation rate immediately in front of and within the gas zone. This is discussed in Section A.6. The overall observable result is a large depression of wall temperature in the freely condensing zone, so that, at first glance, it would appear the gas zone extends much further than is actually true. In terms of gas dissolution analysis, it is very important to properly characterize this interface area so that accurate estimates of gas dissolution phenomena are possible.

The finite difference method used for calculation is useful for interfacing with nodal thermal analyzer programs to obtain the most accurate model of extended surfaces interacting with gas-controlled heat pipes. In addition, the four-level nodal network is very useful for characterizing the overall conductance of heat pipe joints where gas is present. In this case, T_c represents the vapor temperature of the coupled heat pipe.

A.5 EXPERIMENTAL VERIFICATION

Verification of modeling was done with the Freon-22 ($CHClF_2$) heat pipe described in Table A-1. The heat pipe was 96.5 cm long, 1.05 cm inside diameter, and had a wicking consisting of one layer of 200 mesh stainless screen and one layer of 105 mesh stainless screen. The condenser was 27.9 cm long, and was coupled to a commercial fluid cooling system via a cooling bar. The cooling bar and condenser were initially ground flat to ensure uniformity of interfacial heat transfer coefficient. The bar and heat pipe were coated with thermal grease, and coupled together with a 0.0203-cm interfacial acetate sheet for ease in thermal resistance assessment.

Table A-1

GAS-LOADED HEAT PIPE SPECIFICATIONS

Physical Dimensions	1.27 cm sq aluminum extrusion, 1.05 cm inside diameter, length = 96.5 cm
Wicking	1 layer of 200 mesh stainless screen plus one layer of 105 mesh screen on I.D.
Condenser	27.9 cm long, one face ground flat for coupling to coolant bar
Heat Rejection System	Coolant bar coupled to extrusion face with interfacial 0.0203-cm acetate film
Gas Charges	12.2 cc (STP) of helium and xenon

The heat pipe was initially operated over the coolant temperature range -40° to 6°C and 0 to 50 watts, at a reflux head of 4.65 cm, to thermally characterize the heat transfer interfaces at the condensate film, at the pipe/bar interface, and at the bar/coolant channel interface. After thermal characterization, the heat pipe was alternately charged with 12.2 standard cc of helium and xenon, and operated at the same reflux head at coolant temperatures of -41° to 6°C. The temperature profiles established in the condenser were recorded from thermocouple measurements of wall temperature at 2.54 cm intervals. Figures A-2 through A-5 show the profiles recorded with each gas at the two temperatures. The blind or closed end of the heat pipe is at x=0, and vapor flow enters the condenser at x=11 in.

The wall temperature, T_w^*, is defined as

$$T_w^* = \frac{T_w - T_c}{T_{vs} - T_c} \qquad 0 \le T_w^* \le 1 \tag{A-15}$$

Figure A-6 shows actual and predicted performance for the heat pipe when operated at -41°C with helium, at two power levels. Figure A-7 shows the same performance predictions for xenon. Behavior of the helium-loaded pipe is explained well by theory. At the higher power level, the discrepancy of the model and data over a small range is ascribed to chilled condensate flowing countercurrent to vapor in the reflux orientation. However, radial

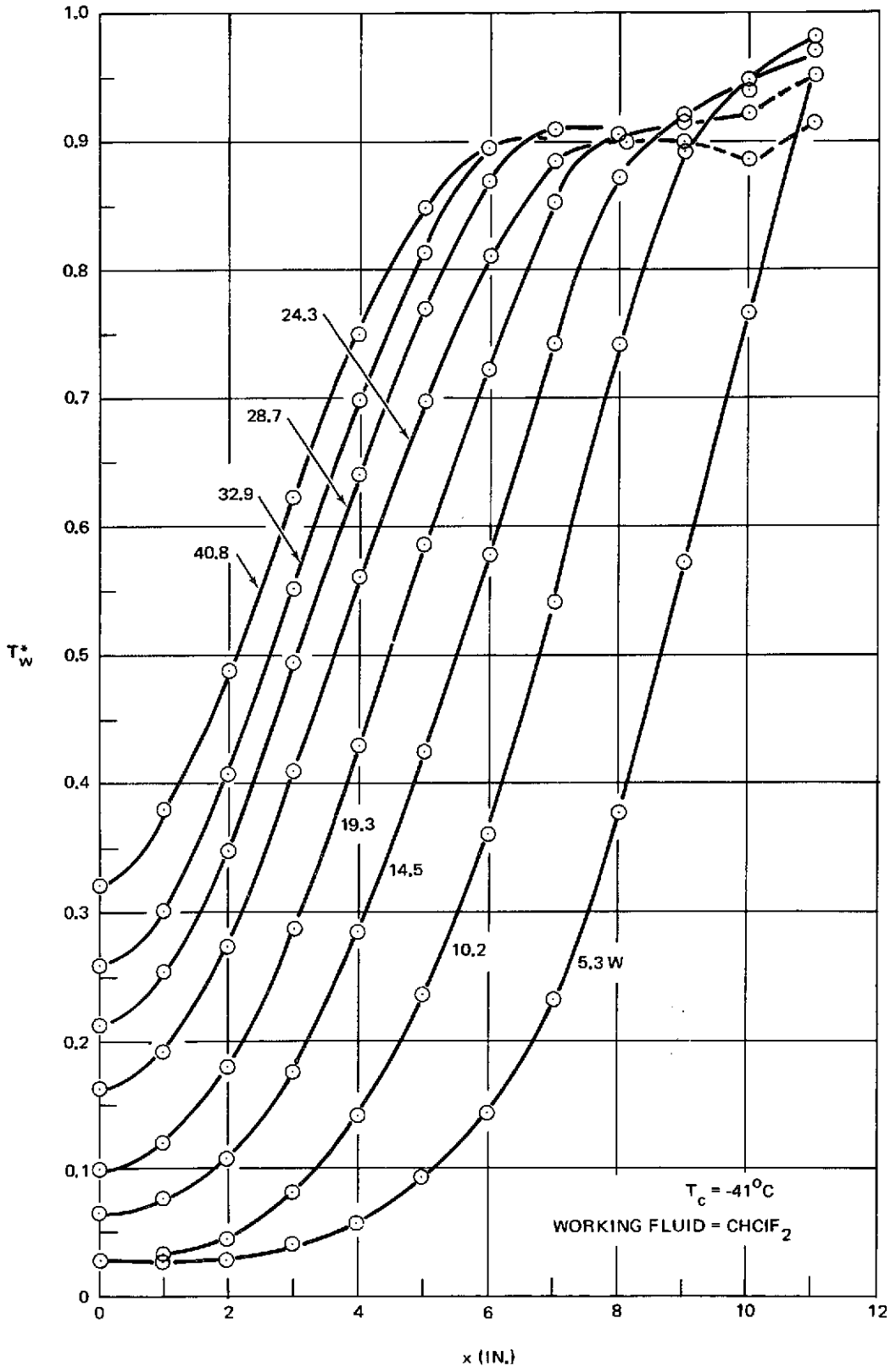

Figure A-2. Experimental Data on the Effect of Helium on Condensation at Low Temperature

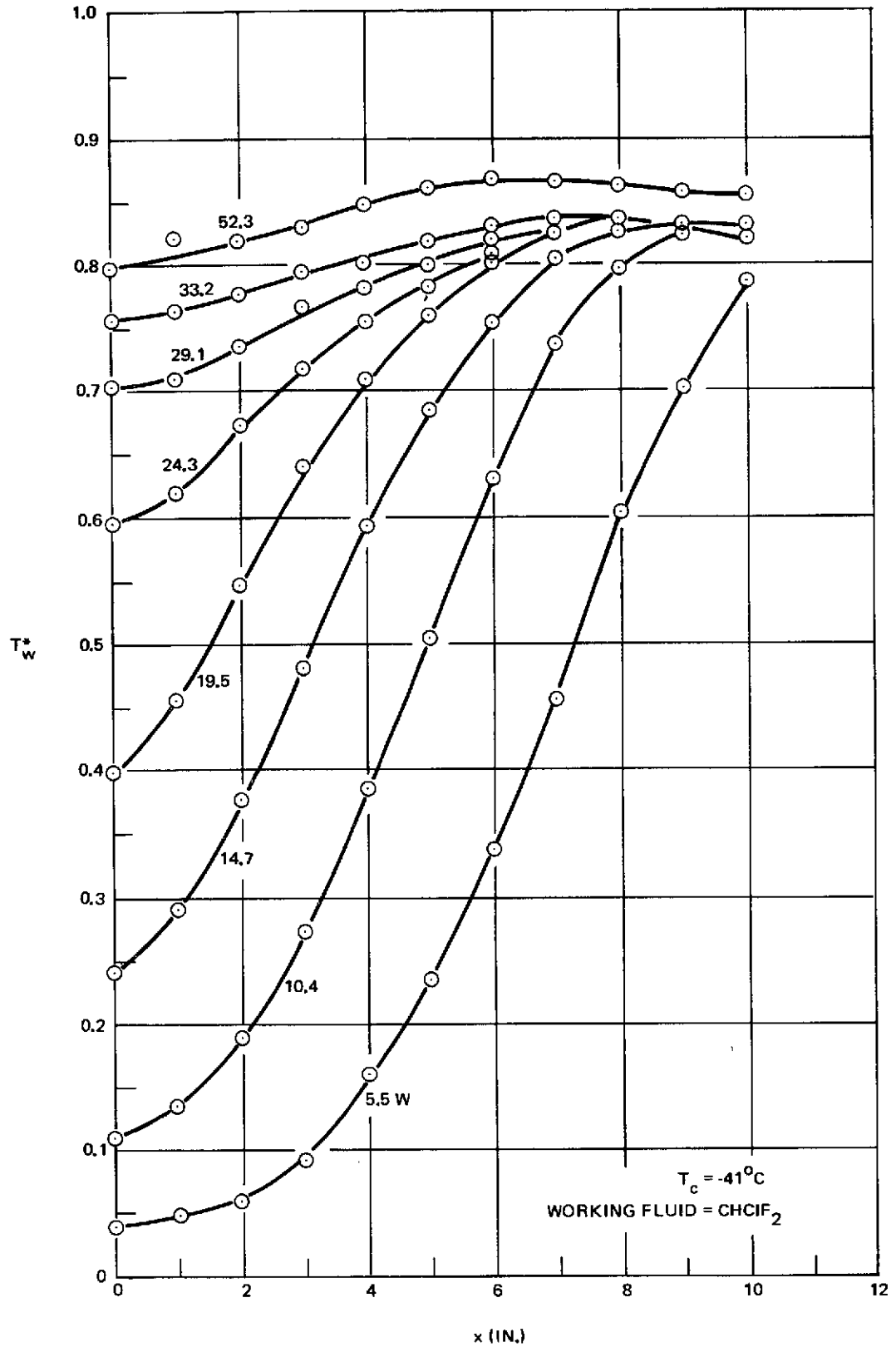

Figure A-3. Experimental Data on the Effect of Xenon on Condensation at Low Temperature

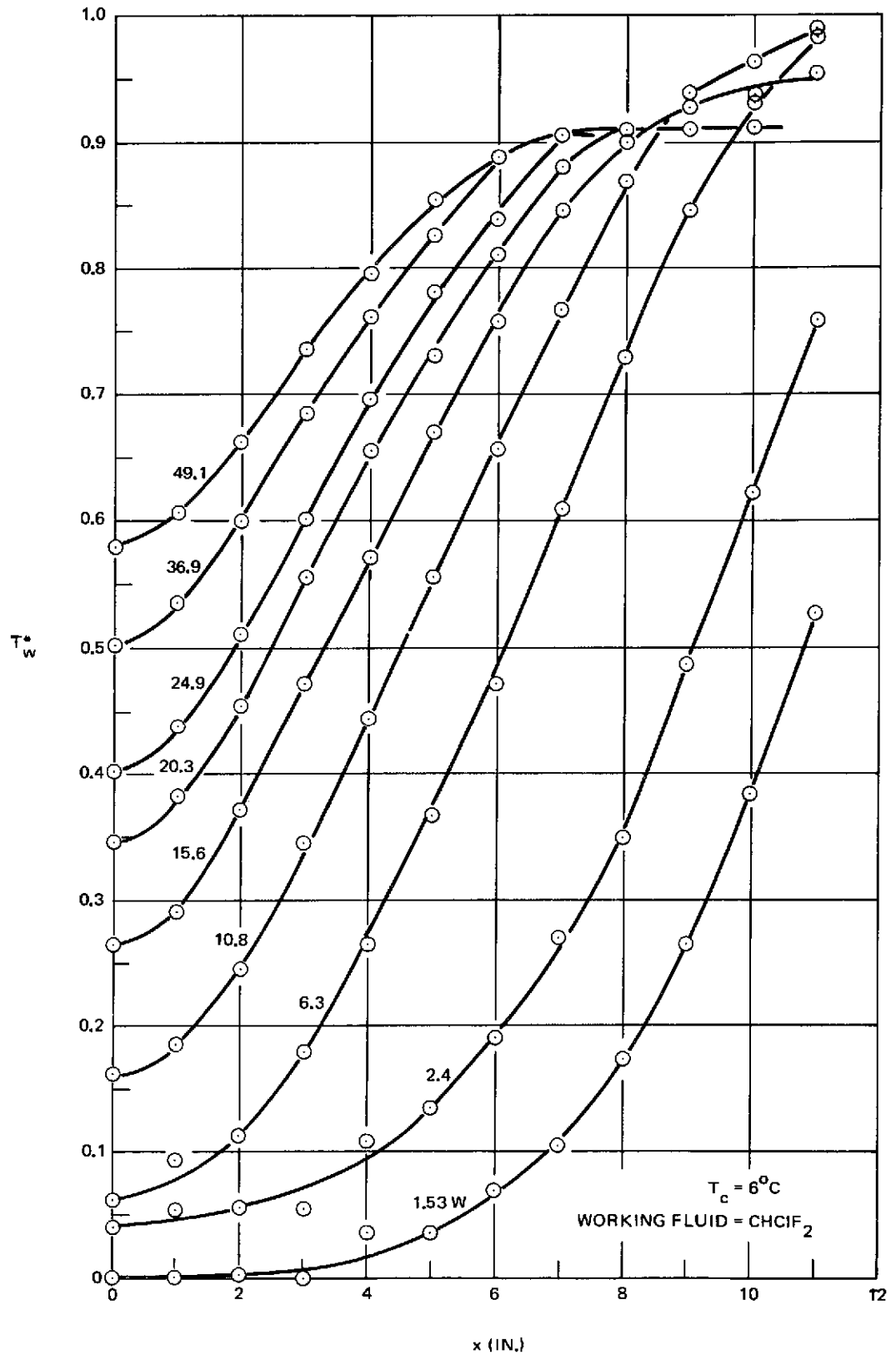

Figure A-4. Experimental Data on the Effect of Helium on Condensation at Moderate Temperature

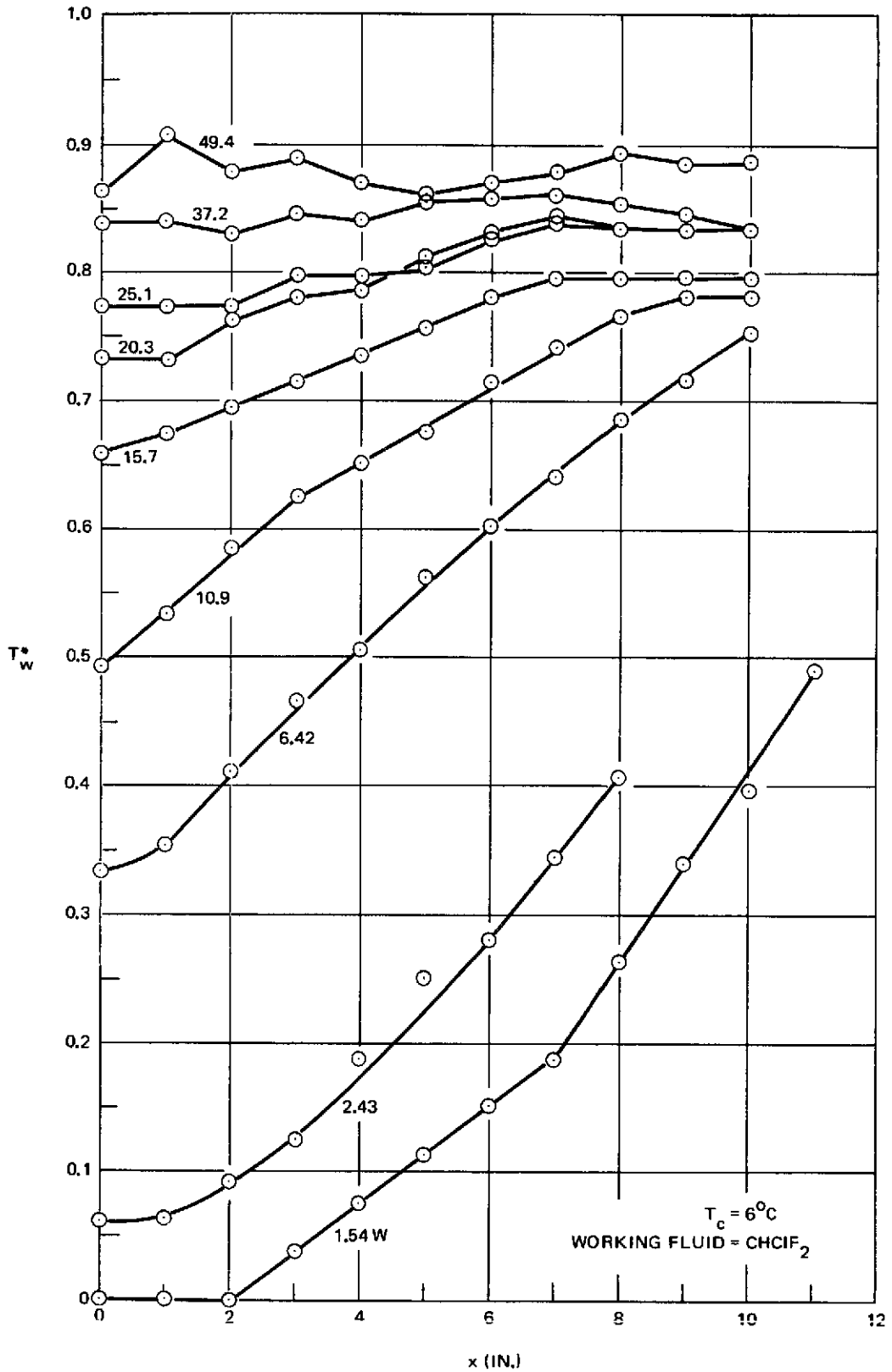

Figure A-5. Experimental Data on the Effect of Xenon on Condensation at Moderate Temperature

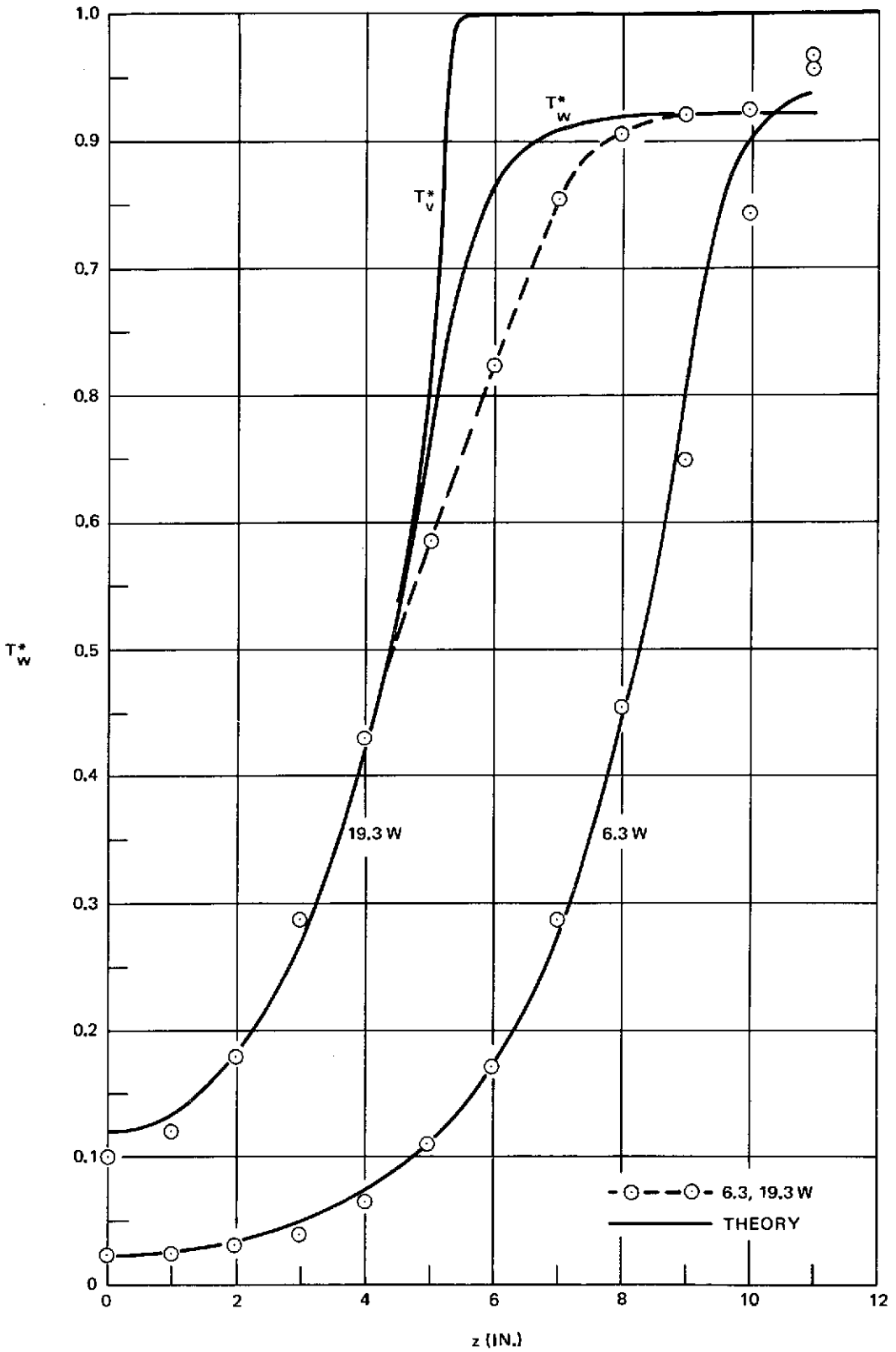

Figure A-6. Wall Temperature Profiles Compared with One-Dimensional Theory (Helium)

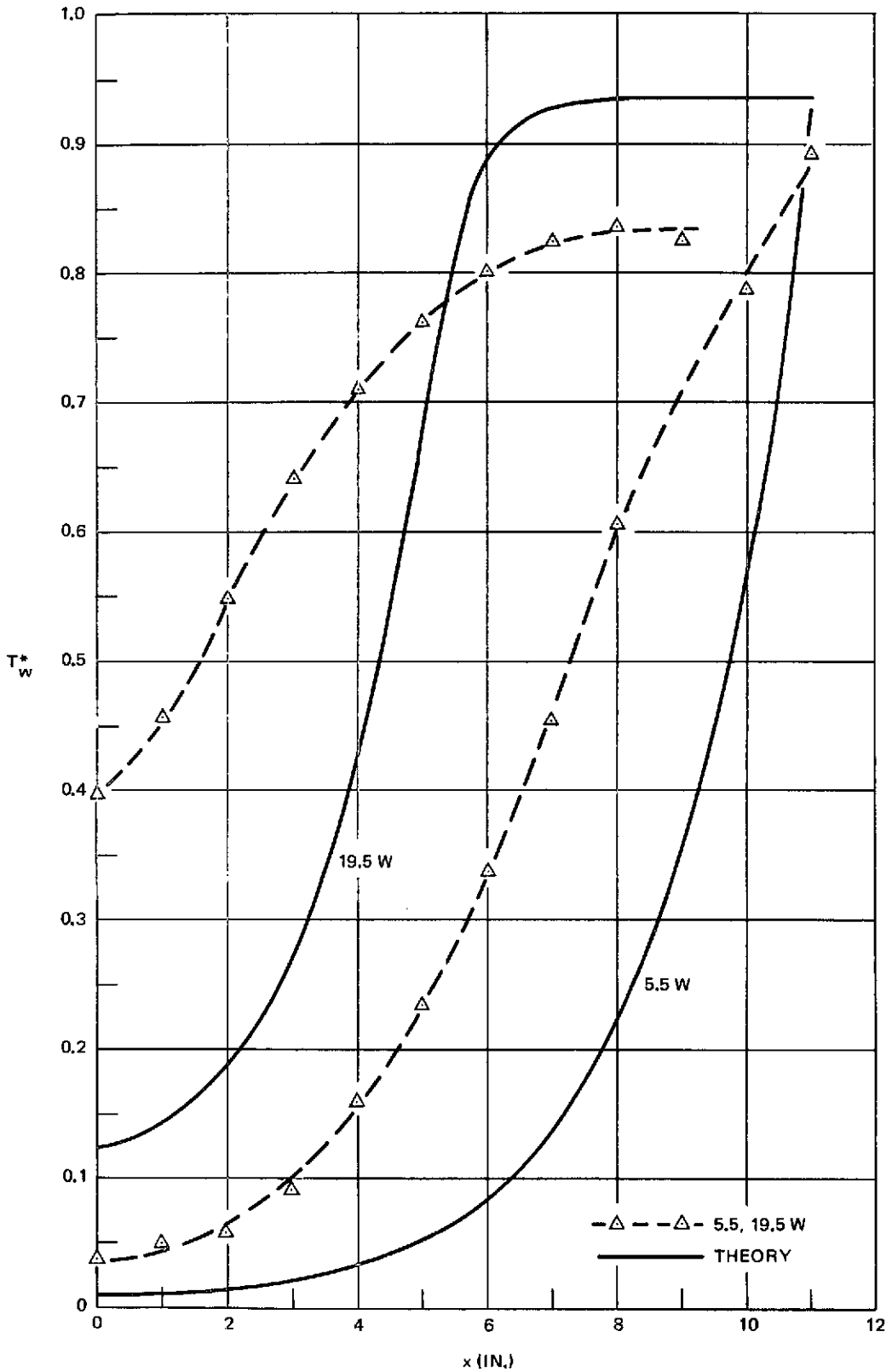

Figure A-7. Wall Temperature Profiles Compared with One-Dimensional Theory (Xenon)

gas gradients could cause such a depression as well, and it is not possible to separate these phenomena at this time. Agreement with xenon data is very poor. This model failure has been identified as resulting from the high solubility of xenon in $CHClF_2$. However, the subject is beyond the scope of this work and will not be discussed. It will be assumed that all gas/liquid combinations discussed are of very low mutual solubility.

Figure A-8 shows the total temperature difference between the heat pipe adiabatic vapor core and the coolant at the two test temperatures. Again, agreement of theory with helium data is satisfactory. However, model calculations for He thermal profiles at 6°C are not in as good agreement with data as at the lower temperature, implying solubility increase with temperature has qualified the assumption of an insoluble gas. The behavior change is shown in Figure A-9, which summarizes the temperature difference between the blind end of the heat pipe and the coolant, as a function of Q. The helium data at low temperature is described well, while the high temperature data is poorly explained, and the xenon data is completely at variance with the model.

In summary, the one dimensional model describes experimental data where gas solubility is adequately low.

A.6 GAS UPTAKE BY CONDENSING FLUID

Dissolved gas in condensate return is intimately coupled to condensation characteristics at the gas zone interface. Sections A.1 through A.5 develop an experimentally supported theory describing heat and mass transfer in the gas zone when gas solubility does not significantly influence mass transfer.

Using the developed model, calculations of gas uptake have been made. Immediately within the gas zone, there exists a region of high condensation rate where gas dissolution is occurring. For the research heat pipe described in Section A.5, the interplay of condensation and heat conduction is shown in Figure A-10. The factor q_c/q_{co} is the ratio of local condensation rate to condensation rate in the gas-free zone with no end effects present. The axial length has been made dimensionless through division by the total condenser length.

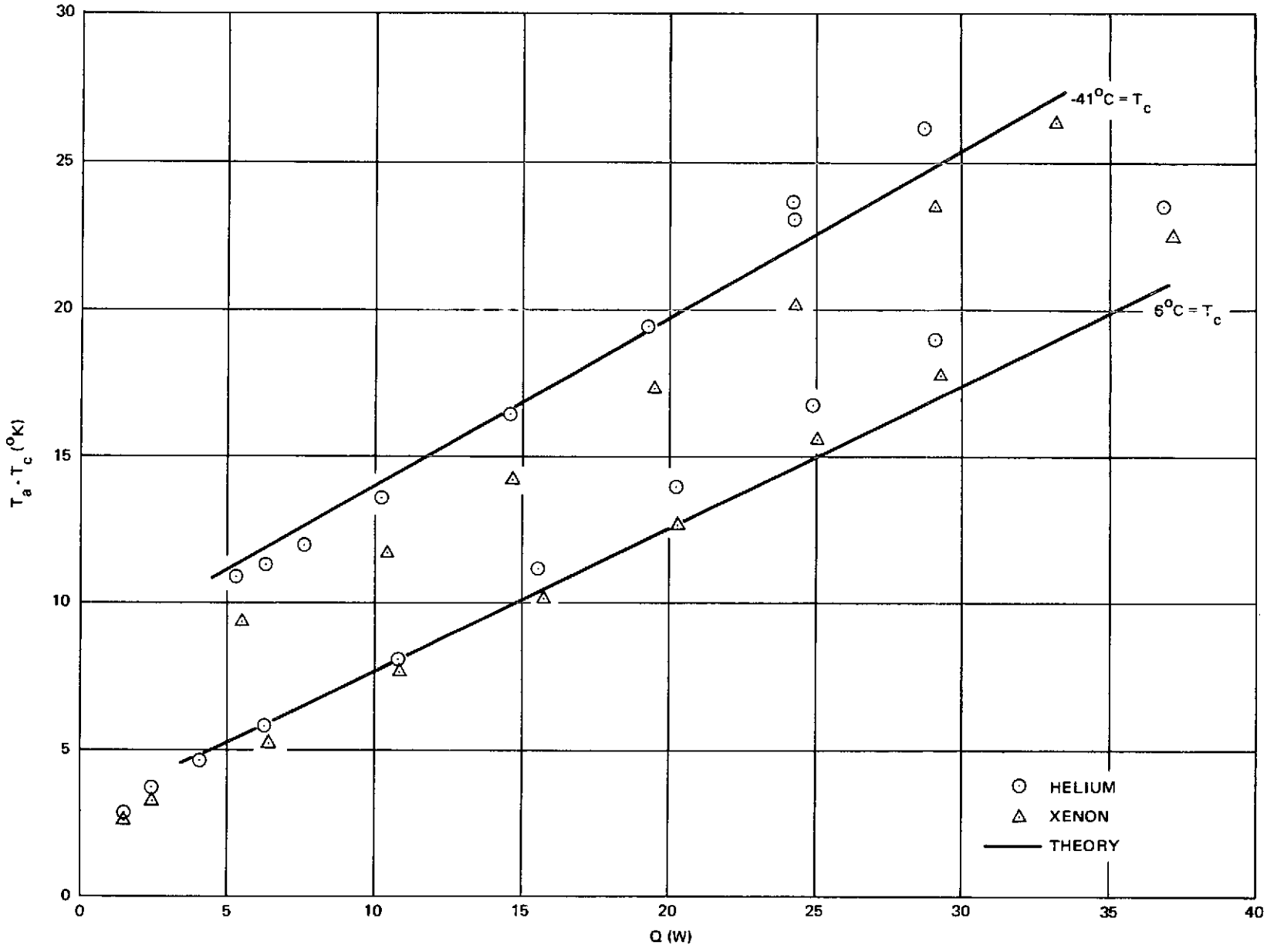

Figure A-8. Total Vapor/Coolant Temperature Difference

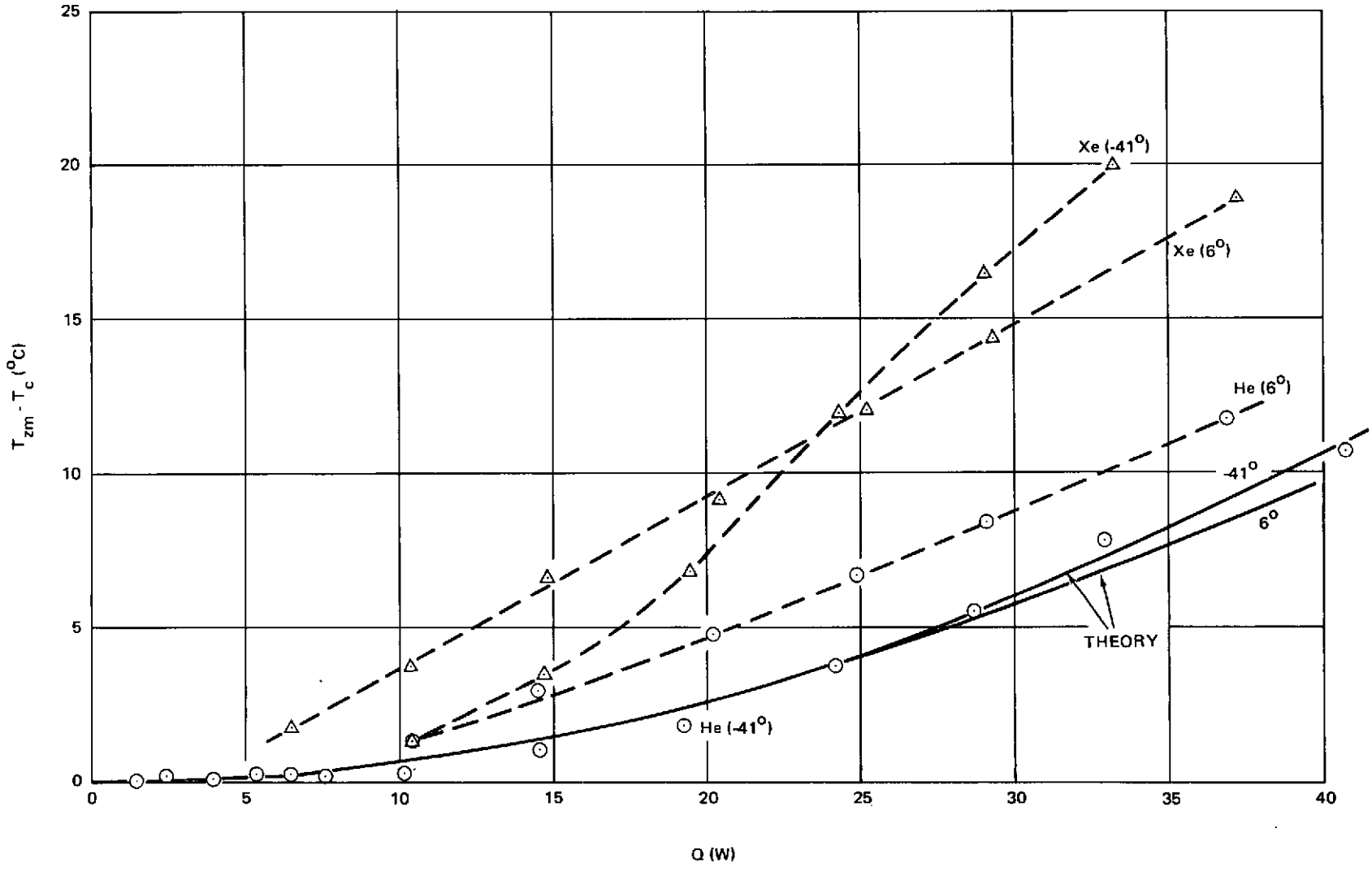

Figure A-9. Temperature Difference for Heat Pipe Blind End

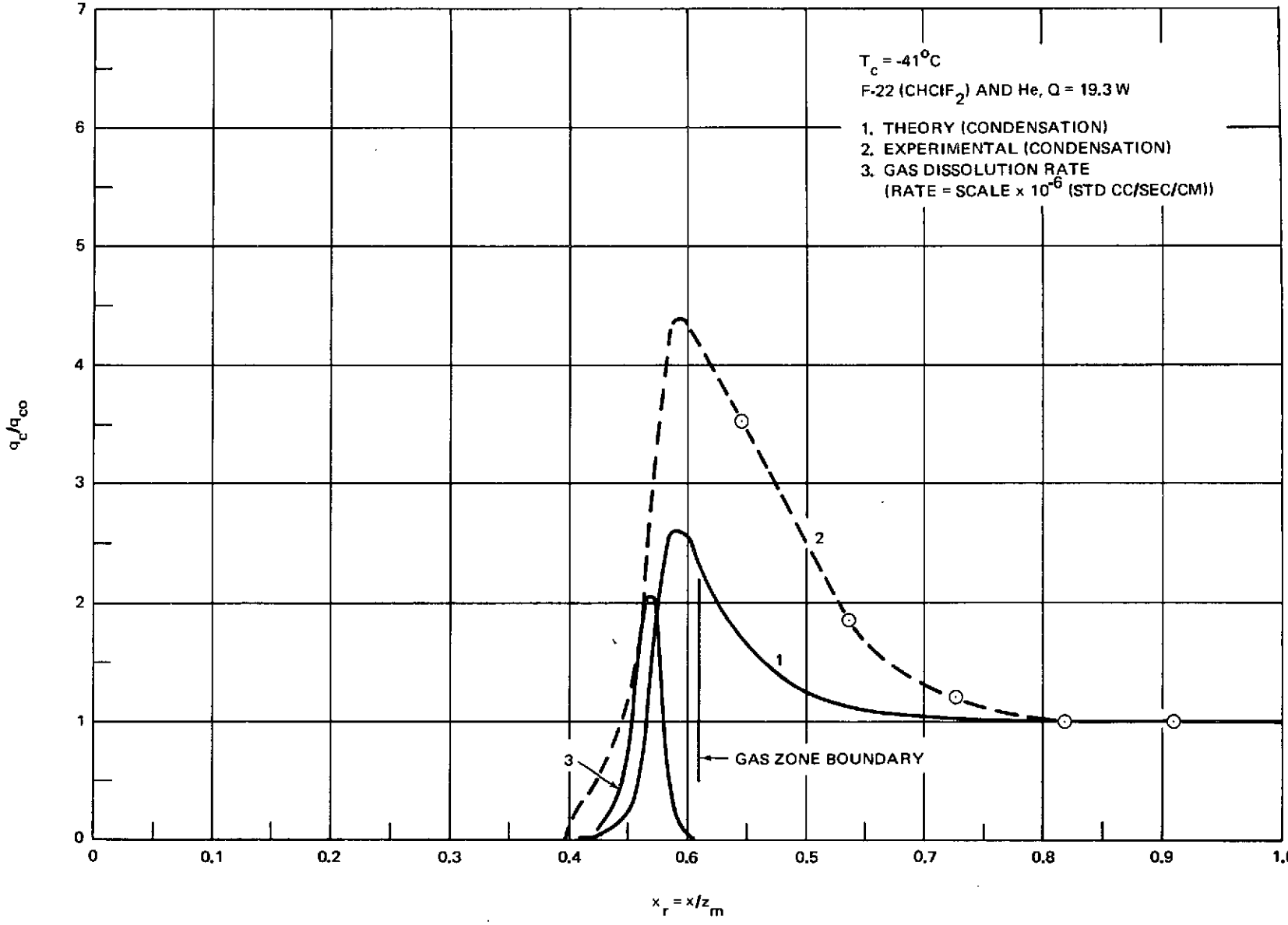

Figure A-10. Condensation Enhancement at the Diffusion Zone

Although the gas front is at $x_r = 0.51$, the actual peak in condensation rate occurs within the gas zone at $x_r = 0.49$. The condensation rate is enhanced by a factor (in theory) of 2.6. This is a remarkable and unexpected situation. However, the reason for this behavior is not difficult to understand. In the gas interface region, the one dimensional heat conduction process is suddenly a two-dimensional process due to axial conduction to the chilled gas leg augmenting the standard conduction process perpendicular to the heat transfer interfaces. Therefore, the wall temperature is depressed and condensation onto the fluid film increases considerably.

Also shown in Figure A-10 is the condensation rate indicated by using experimental wall temperatures and the theoretical vapor temperature shown in Figure A-5. The general shape of this curve is in agreement with the totally analytic estimate, and condensation in the stagnant gas leg extends over approximately the same zone as predicted by theory. It is believed the high apparent condensation rates for the experimental data are due to return condensate flow, since testing was done in reflux. The actual wall temperatures reflect not only local condensation but fluid flow from cooler areas at higher elevation. If radial concentration gradients existed in this diffuse zone, however, it would not be possible to distinguish in this experiment whether the temperature depression was due to fluid flow or a radial gas layer. At present the fluid flow effect appears to be in better qualitative agreement.

In the modeling of gas uptake, it is assumed that, in the gas contaminated zone, condensate leaves the zone with an equilibrium amount of noncondensable gas in solution, and that this fluid mixes completely with condensate from the remainder of the condenser. The total amount of gas taken into solution is calculated by integrating over the condensation profile using the local gas partial pressure to determine gas uptake through Henry's Law. The local rate of gas dissolution for this heat pipe is shown in Figure A-10 as Curve 3.

A.7 REFERENCES

A-1. B.D. Marcus, Theory and Design of Variable Conductance Heat Pipes, NASA Report CR-2018 (April 1972).

A-2. R. Reid and T. Sherwood, The Properties of Gases and Liquids, McGraw-Hill (1966).

Appendix B
STEADY-STATE OCCLUSION LENGTH

Under isothermal conditions, mathematical models of occlusion length are possible for the quasi-steady-state condition where the uptake of noncondensable gas by the occlusion from condensate equals the diffusional loss rate through the radial fluid film around the occlusion. That is, there is a dynamic equilibrium between gas input and loss mechanisms. The model derived relates gas input to film diffusion through the artery envelope and to the available occlusion length for diffusion, ℓ_b, under isothermal conditions.

The model used is shown in Figure B-1. Dissolved gases are transported to the end cap and axially through the fluid film by condensate flow. Because the end cap defines an area of flow stagnation, it is assumed that dominant communication of condensate with the occlusion core is by way of contact over the cylindrical surface. Because no pressure drops are probable within the occlusion under isothermal conditions, the partial pressure of noncondensable gas within the occlusion is a constant and the internal surface of the fluid film is at a saturation concentration C_{gb}. The external film surface is at equilibrium with gas content in the vapor phase at C_{gf}. Because the fluid film surrounding the occlusion is actually a lattice filled with fluid, it can be assumed that plug-flow occurs in the porous envelope, and diffusion of gases can be treated with a Cartesian coordinate slab model. At $z = 0$, the condensate is gas-saturated at a level C_{gr}, equivalent to mole fraction $\eta x_{g\ell}$, as defined in Section 2.

If the coordinate system shown in Figure B-1 is adopted, and axial diffusion neglected, then conservation of dissolved gas in the liquid yields

$$\frac{\partial C_g}{\partial z} = \frac{D'}{\bar{v}} \frac{\partial^2 C_g}{\partial y^2} \qquad \text{(adiabatic)} \qquad \text{(B-1)}$$

$$\frac{(\ell_b - z)}{\ell_e} \frac{\partial C_g}{\partial z} = \frac{D'}{\bar{v}_m} \frac{^2C_g}{y^2} = \omega \frac{\partial^2 C_g}{\partial y^2} \qquad \text{(evaporator)} \qquad \text{(B-2)}$$

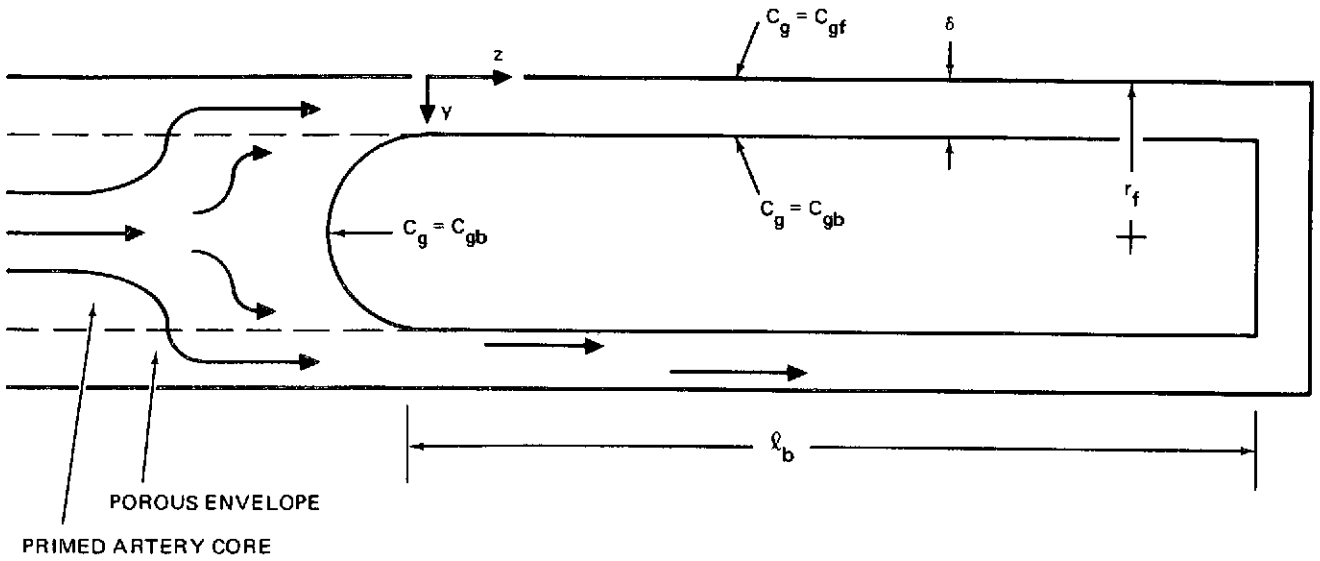

Figure B-1. Steady-State Occlusion Model Incorporating Gas Diffusion

where C_g denotes gas concentration and $\bar{v}$ is the average fluid velocity in the occlusion film envelope. Flow velocity $\bar{v}_m$ is the fluid film velocity for the case that the occlusion length equals ℓ_e, the evaporator length. The diffusion coefficient D' is an effective value reflecting the lattice structure of typical arterial walls (Reference B-1). An analytic solution to Equation B-1 is possible by separation of variables, and a stability criterion can be developed. The solution shows interaction of flow and diffusion, although it is not strictly valid for the evaporator. A dimensionless concentration is defined as

$$C^* = \frac{C_g - C_{gf}}{C_{gb} - C_{gf}} \qquad \text{(B-3)}$$

where subscripts b and f correspond to the internal and external film surfaces, respectively. The solution to Equation B-1, with $C^* = C^*_r$ at $z = 0$, is composed of a steady-state solution plus a transient series solution.

$$C^* = \frac{y}{\delta} + \frac{2}{\pi} \sum_{N=1}^{\infty} \frac{\left[C_r^* (1-(-1)^N) + (-1)^N\right]}{N} \quad EXP(-N^2 \omega z) \sin(N\pi y/\delta) \qquad (B-4)$$

where δ is the fluid film thickness and the reciprocal relaxation length $\omega = \pi^2 D'/\bar{v}\delta^2$. At steady-state, all diffusive mass flow of noncondensable gas to the occlusion must sum to zero. The overall rate over the cylindrical section can be found by evaluating the diffusion gradient of Equation B-4 at $y = \delta$, and then integrating over the range $0 \leq z \leq \ell_b$. Setting this integral equal to zero yields the following equality for a diffusion-stable occlusion which is neither growing or collapsing with time.

$$\frac{\omega \ell_b}{2} = \sum_{N=1}^{\infty} \frac{\left[C_r^* (1 - (-1)^N) - 1\right]}{N^2} \quad (1 - EXP(-N^2 \omega \ell_b)) \qquad (B-5)$$

Equation B-5 provides a relationship between the factor $\omega \ell_b$ and C_r^*. C_r^* is given by

$$C_r^* = \frac{C_{gr} - C_{gf}}{C_{gb} - C_{gf}} \qquad (B-6)$$

Table B-1

DIMENSIONLESS LENGTH $\omega \ell_b$ vs C_r^*

C_r^*	$\omega \ell_b$
1.	0
1.01	0.79
1.025	1.02
1.05	1.29
1.20	2.37
2.0	6.56
4.0	16.43
6.0	26.29
9.0	36.14
10.0	46.0

Table B-1 gives values of the factor $\omega \ell_b$ as a function of C_r^*. For C_r^* greater than 1.2, the solution for ℓ_b is very close to

$$\ell_b = \frac{\bar{v}\delta^2}{2D'} \left(C_r^* - \frac{2}{3} \right) \qquad C_r^* \geq 1.2 \qquad \text{(B-7)}$$

For many artery structures, $\bar{v} \sim 1$ cm/sec, $\delta \sim 0.02$ cm, and $D' \sim 5\,(10^{-5})$ cm^2/sec. If C_r^* equaled 1.2, then ℓ_b would be on the order of 2 cm in length.

REFERENCE

1. E. W. Saaski. Investigation of Bubbles in Arterial Heat Pipes. NASA CR 114, 531, 1972.